

Gravitational wave and Collider searches for the EWSB patterns

Ligong Bian^{1,2,*} Huai-Ke Guo^{3,†} Yongcheng Wu^{4,‡} and Ruiyu Zhou^{1,§}

¹ *Department of Physics, Chongqing University, Chongqing 401331, China*

² *Department of Physics, Chung-Ang University, Seoul 06974, Korea*

³ *Department of Physics and Astronomy, University of Oklahoma, Norman, OK 73019, USA*

⁴ *Ottawa-Carleton Institute for Physics, Carleton University,
1125 Colonel By Drive, Ottawa, Ontario K1S 5B6, Canada*

(Dated: November 27, 2024)

We study the Electroweak symmetry breaking mechanism with extra Electroweak symmetry breaking contributions (eEWSB) that are bounded by the Fermi constant and limits from the related collider searches. The eEWSB is helpful to build a different zero temperature vacuum structure from the Standard Model (SM), and therefore leads to different Electroweak phase transition patterns at the early Universe. We investigate the collider search prospects and gravitational waves (GW) predictions from the strongly firstly order phase transition (SFOEWPT) in this scenario. The Higgs pair searches at lepton colliders are found to be complementary with the GW searches of the SFOEWPT parameter spaces.

* lgbycl@cqu.edu.cn

† ghk@ou.edu

‡ ycwu@physics.carleton.ca

§ zhoury@cqu.edu.cn

CONTENTS

I. Introduction	2
II. The EWPT dynamics and methodology	3
A. On the vacuum structures and the possible EWPT patterns	3
B. Phase transition dynamics	5
III. The SFOEWPT and Higgs phenomenology	8
IV. Gravitational wave searches	14
V. Collider Searches	19
VI. Conclusions	25
Acknowledgment	26
A. The GM model	27
B. EWPT in the SM + Real Singlet: xSM model	29
C. The h^6 operator for GM and xSM models	29
D. Some Couplings in GM model	34
References	36

I. INTRODUCTION

The observation of the SM Higgs at 126 GeV at LHC [1, 2] is a milestone of the particle physics, which means that the W and Z boson obtain their masses through the Electroweak symmetry breaking (EWSB) mechanism. The cubic and quartic Higgs couplings are supposed to be crucial to reveal the Higgs potential shape and the EWSB mechanism. The sensitivity of measurement of these couplings at LHC is pretty low, while future precision measurements are able to tell if there are new physics beyond the Standard Model (SM) that could drive deviation of the EWSB and how large the deviation could be. The observation of gravitational waves from the Binary Black hole merger by the LIGO and Virgo collaborations [3] opens a new era to search for fundamental physics. An important category of gravitational waves is a stochastic background [4] originated from the earth Universe. One important source of this kind is a strongly first order Electroweak phase transition (SFOEWPT), which gives a dynamical explanation of the EWSB as the Universe cools down, and is a crucial ingredient in the explanation of the baryon asymmetry of the Universe within the Electroweak baryogenesis mechanism.¹

New physics that takes part in the Electroweak phase transition process may or may not contribute an extra component of EWSB contribution. For example, the SM plus real singlet model (xSM) has been extensively studied where the singlet scalar do not contribute any EWSB contribution (see Ref. [7] for a recent study). Meanwhile, the triplets in the Georgi-Machacek (GM) model, as will be studied in this work, can indeed contribute to the EWSB. Though both of the two models share the same vacuum structure topology, the triplets contribution to the EWSB, i.e. the extra EWSB contribution, is bounded by the Fermi constant and gauge boson related collider searches. Therefore, one can expect different collider phenomenology, different SFOEWPT behavior and thus different gravitational wave signal predictions for different amount of the extra EWSB contributions.

The zero temperature vacuum structure with extra local minimum in addition to the Electroweak vacuum could yield the possibility of multi-step phase transition as well as one-step phase transition. In Ref. [8, 9], the relation between the zero temperature potential difference and the SFOEWPT condition has been studied within the 2HDM. For previous studies of multi-step phase transition and related vacuum structure at zero temperature, we refer to Ref. [7, 10–17]. In this work, we use the Georgi-Machacek model to reveal that, the extra EWSB contribution can induce one-step or two-step SFOEWPT depending on the vacuum structure that has been studied previously by us in Ref [18]. The one-step SFOEWPT occurs with the symmetry change from $SU(2)_L \times SU(2)_R$ to the phase where Electroweak symmetry is broken. The two-step SFOEWPT occurs with the first-step being the symmetry change of $SU(2)_L \times SU(2)_R \rightarrow SU(2)_V$, and the following second step being the dynamical broken of the Electroweak symmetry. In this work we improved the algorithm for the calculation of the critical order parameters of the phase transition. We further evaluate the gravitational wave signals being generated during the SFOEWPT. In comparison with the one-step situation, the gravitational wave signal spectrum generated from

¹ The SFOEWPT is one of the three Shakharov conditions [5] that quenches the sphaleron process inside the bubble and therefore preserve the baryon asymmetry being generated (see Ref. [6] for a recent review on Electroweak baryogenesis).

two-step SFOEWPT is found much easier to be probed by the projected space-based interferometers, such as: LISA [19], BBO, DECIGO (Ultimate-DECIGO) [20], TianQin [21] and Taiji [22] programs. This is significantly different from the xSM case as was studied in Ref. [7], where the vacuum expectation value (VEV) of the extra singlet is more free from the limits of the collider searches.

This work is organized as follows: The vacuum structure analysis and the phase transition calculation approach are given in Section II. In Section III, we show the relation between the phase transition and the collider phenomenology, and demonstrate how these two interplay on the extra EWSB contributions. The gravitational wave signal predictions from the one-step and two-step SFOEWPT are investigated in Section IV. The collider search prospects for the SFOEWPT valid regions are addressed in Section V. We finally conclude with Section VI. Some details about the model are listed in Appendix.

II. THE EWPT DYNAMICS AND METHODOLOGY

In this section, we first develop the methods for vacuum structure analysis and phase transition critical order parameter analysis, which can be applied to phase transition analysis of any multi-scalar models, such as xSM, 2HDM, 2HDM+S, NMSSM, etc. In the GM model, at the critical temperature, the strongly first order phase transition condition could be fulfilled when $v_c/T_c \equiv \sqrt{h_\phi(T_c)^2 + 8h_\xi(T_c)^2}/T_c \geq 1$ [18, 23].

A. On the vacuum structures and the possible EWPT patterns

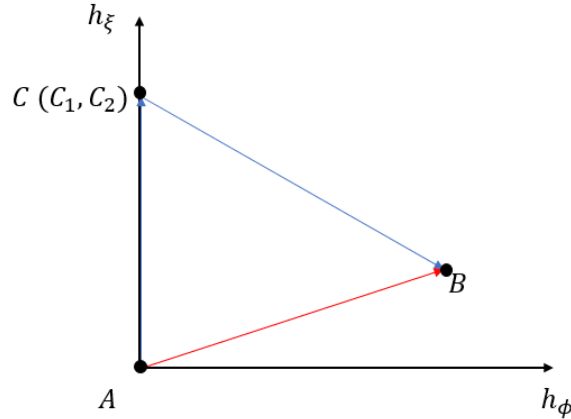


FIG. 1. The vacuum structure in GM model.

The leading order zero temperature effective potential of the GM model is [18]

$$V_0 = \frac{1}{4}(4h_\phi^4\lambda_1 + 2(h_\xi^2 + h_\chi^2)(m_2^2 + 2\lambda_2(h_\xi^2 + h_\chi^2)) + 2\lambda_3(2h_\xi^4 + h_\chi^4) + h_\phi^2(2m_1^2 + 4\lambda_4h_\xi^2 + h_\xi(2\sqrt{2}\lambda_5h_\chi + \mu_1) + h_\chi(4\lambda_4h_\chi + \lambda_5h_\chi + \sqrt{2}\mu_1)) + 12\mu_2h_\xi h_\chi^2) . \quad (1)$$

For the vacuum structure studies, we impose $h_\chi = \sqrt{2}h_\xi$ as required by the custodial symmetry, which ensures $\rho = 1$ at leading order. The general vacuum structure determined by the above potential is shown in Fig. 1, where A is the $(h_\phi, h_\xi) = (0, 0)$ vacuum, B is the desired EW vacuum, $C_{1,2}$ are the alternative vacuums with $h_\phi = 0$ (the $SU(2)_V$ vacuum). In this paper we consider the case where there are two possible C points in GM model which can be expressed as below,

$$C_{1(2)} \text{ point} : h_\phi \rightarrow 0, h_\xi \rightarrow \frac{-3\mu_2 \pm \sqrt{-12m_2^2\lambda_2 - 4m_2^2\lambda_3 + 9\mu_2^2}}{4(3\lambda_2 + \lambda_3)} . \quad (2)$$

The scalar potential at the EW vacuum (B) should be the global minimum one and the value of the scalar potential at the original point is the maximal one of these three. The scalar potential at these three different vacuum points, $V_0(A)$, $V_0(B)$, $V_0(C_{1(2)})$, are

$$\begin{aligned} V_0(A) &= 0 , \\ V_0(B) &= -\lambda_1 v_\phi^4 - 3v_\xi^3(\mu_2 + (3\lambda_2 + \lambda_3)v_\xi) - \frac{3}{8}v_\xi(\mu_1 + 4(2\lambda_4 + \lambda_5)v_\xi)v_\phi^2 , \\ V_0(C_{1(2)}) &= -\frac{3}{256v_\xi(3\lambda_2 + \lambda_3)^3}(F \mp 3\mu_2)^2(\mu_2(24v_\xi^2(3\lambda_2 + \lambda_3) \mp 2v_\xi F) \\ &\quad + (3\lambda_2 + \lambda_3)(16v_\xi^3(3\lambda_2 + \lambda_3) + v_\phi^2(4v_\xi(2\lambda_4 + \lambda_5) + \mu_1)) \\ &\quad + 6\mu_2^2v_\xi) , \end{aligned} \quad (3)$$

where

$$F = \left(\frac{v_\phi^2(3\lambda_2 + \lambda_3)(4v_\xi(2\lambda_4 + \lambda_5) + \mu_1)}{v_\xi} + (4v_\xi(3\lambda_2 + \lambda_3) + 3\mu_2)^2 \right)^{1/2} . \quad (4)$$

The one-step phase transition would take place when $V_0(A) > V_0(B)$ ($\Delta V_0(AB) > 0$) and $-12m_2^2\lambda_2 - 4m_2^2\lambda_3 + 9\mu_2^2 < 0$. Meanwhile, the two-step phase transition might happen when $-12m_2^2\lambda_2 - 4m_2^2\lambda_3 + 9\mu_2^2 \geq 0$ and $V_0(A) > V_0(C_{1(2)}) > V_0(B)$ (with $\Delta V_0(AC_{1(2)}) > 0, \Delta V_0(C_{1(2)}B) >$

0). The potential differences are given as

$$\begin{aligned}\Delta V_0(AB) &\equiv V_0(A) - V_0(B) \\ &= \lambda_1 v_\phi^4 + 3v_\xi^3(\mu_2 + (3\lambda_2 + \lambda_3)v_\xi) + \frac{3}{8}v_\xi(\mu_1 + 4(2\lambda_4 \\ &\quad + \lambda_5)v_\xi)v_\phi^2, \end{aligned} \quad (5)$$

$$\begin{aligned}\Delta V_0(AC_{1(2)}) &\equiv V_0(A) - V_0(C_{1(2)}) \\ &= \frac{3}{256v_\xi(3\lambda_2 + \lambda_3)^3}(F \mp 3\mu_2)^2(\mu_2(24v_\xi^2(3\lambda_2 + \lambda_3) \\ &\quad \mp 2v_\xi F) + (3\lambda_2 + \lambda_3)(16v_\xi^3(3\lambda_2 + \lambda_3) \\ &\quad + v_\phi^2(4v_\xi(2\lambda_4 + \lambda_5) + \mu_1)) \\ &\quad + 6\mu_2^2 v_\xi), \end{aligned} \quad (6)$$

$$\begin{aligned}\Delta V_0(C_{1(2)}B) &\equiv V_0(C_{1(2)}) - V_0(B) \\ &= -\frac{3}{256v_\xi(3\lambda_2 + \lambda_3)^3}(F \mp 3\mu_2)^2(\mu_2(24v_\xi^2(3\lambda_2 + \lambda_3) \\ &\quad \mp 2v_\xi F) + (3\lambda_2 + \lambda_3)(16v_\xi^3(3\lambda_2 + \lambda_3) \\ &\quad + v_\phi^2(4v_\xi(2\lambda_4 + \lambda_5) + \mu_1)) \\ &\quad + 6\mu_2^2 v_\xi) + \lambda_1 v_\phi^4 + 3v_\xi^3(\mu_2 + (3\lambda_2 + \lambda_3)v_\xi) \\ &\quad + \frac{3}{8}v_\xi(\mu_1 + 4(2\lambda_4 + \lambda_5)v_\xi)v_\phi^2, \end{aligned} \quad (7)$$

$$\begin{aligned}\Delta V_0(C_1 C_2) &\equiv V_0(C_1) - V_0(C_2) \\ &= \frac{3\mu_2 F^3}{16(3\lambda_2 + \lambda_3)^3}. \end{aligned} \quad (8)$$

The $\Delta V_0(C_1 C_2)$ determines the detailed phase transition patterns in the two-step phase transition scenario, as will be explored latter.

B. Phase transition dynamics

With the zero temperature scalar potential at hand, the phase transition dynamics can be estimated with the finite temperature potential using the gauge invariant approach [24],

$$V_T = V_0 + \frac{1}{2}c_\phi T^2 h_\phi^2 + \frac{1}{2}c_\xi T^2 h_\xi^2 + \frac{1}{2}c_\chi T^2 h_\chi^2, \quad (9)$$

with V_0 being given in Eq. (1), and the finite temperature corrections being

$$\begin{aligned}c_\phi &= \frac{3g^2}{16} + \frac{g'^2}{16} + 2\lambda_1 + \frac{3\lambda_4}{2} + \frac{1}{4}y_i^2 \sec^2 \theta_H, \\ c_\xi &= \frac{g^2}{2} + \frac{11\lambda_2}{3} + \frac{7\lambda_3}{3} + \frac{2\lambda_4}{3}, \\ c_\chi &= \frac{g^2}{2} + \frac{g'^2}{4} + \frac{11\lambda_2}{3} + \frac{7\lambda_3}{3} + \frac{2\lambda_4}{3}. \end{aligned} \quad (10)$$

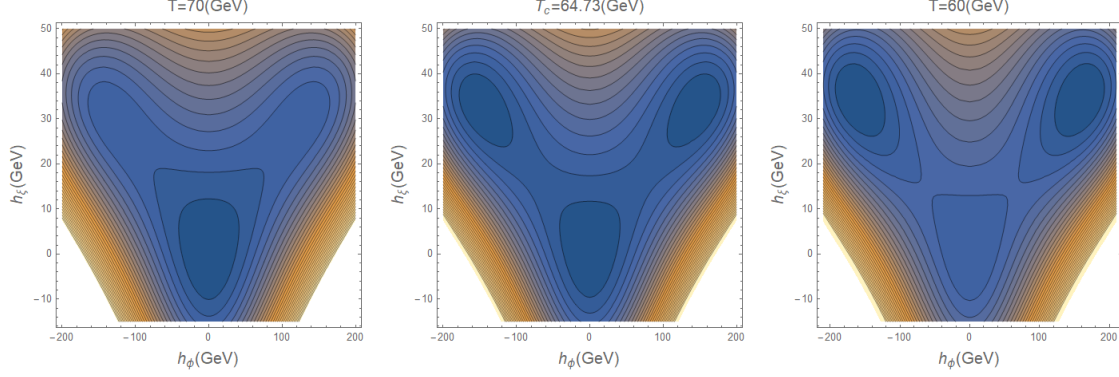


FIG. 2. The contours of V_T in h_ϕ - h_ξ plane, with the parameters being: $\lambda_1 = 0.035$, $\lambda_2 = 0.574$, $\lambda_3 = -0.547$, $\lambda_4 = 0.798$, $\lambda_5 = 1.908$, $\theta_H = 0.273$, $\mu_1 = -360.373$ GeV, $\mu_2 = -47.377$ GeV.

For the safety of custodial symmetry, we assume $h_\chi = \sqrt{2}h_\xi$ for phase transition studies. In the one-step phase transition situation, the phase transition occurs through the path of $A \rightarrow B$ directly with $h_{\phi,\xi}^B$ locating around $v_{\phi,\xi}$ at finite temperature T_C . The phase transition may occur after the temperature drops below the T_C . In Fig. 2, we illustrate the one-step phase transition process as the temperature drops. The global minimum of the finite temperature potential V_T changes from the A to the B , through which one obtains the EW symmetry breaking minimum.

As for the two-step phase transition scenario, the condition for the first step of the two-step phase transition (A point \rightarrow C point) can be written as:

$$V_T(0,0,T_{1C}) = V_T(0,h_\xi^{1C},T_{1C}), \quad \left. \frac{dV_T(h_\phi,h_\xi,T_{1C})}{dh_\xi} \right|_{h_\phi=0,h_\xi=h_\xi^{1C}} = 0. \quad (11)$$

The critical parameters h_ξ^{1C} and T_{1C} are calculated as,

$$h_\xi^{1C} = -\frac{\mu_2}{3\lambda_2 + \lambda_3}, \quad T_{1C} = \frac{\sqrt{-3m_2^2(3\lambda_2 + \lambda_3) + 6\mu_2^2}}{\sqrt{(c_\xi + 2c_\chi)(3\lambda_2 + \lambda_3)}}. \quad (12)$$

For the second-step of the two-step phase transition to occur, the following degeneracy conditions at the critical temperature are necessary,

$$V_T(0,h_\xi^C,T_C) = V(h_\phi^B,h_\xi^B,T_C), \quad \left. \frac{dV_T(h_\phi,h_\xi,T_C)}{dh_\phi} \right|_{h_\phi=h_\phi^B,h_\xi=h_\xi^B} = 0, \quad \left. \frac{dV_T(h_\phi,h_\xi,T_C)}{dh_\xi} \right|_{h_\phi=h_\phi^B,h_\xi=h_\xi^B} = 0, \quad \left. \frac{dV_T(0,h_\xi,T_C)}{dh_\xi} \right|_{h_\xi=h_\xi^C} = 0, \quad (13)$$

through which the critical temperature and critical field value can be obtained. For the two-step case, using the determinant of the Hessian matrix (at both the zero temperature and the finite temperature) to ensure the two degenerate vacua occur, the following conditions need to be satisfied:

$M_{3(5,6)}P_{3(5,6)} - N_{3(5,6)}^2 > 0, M_{3(5,6)} > 0$, with

$$\begin{aligned} \frac{d^2V_0(h_\phi, h_\xi)}{dh_\phi^2} \Big|_{h_\phi=v_\phi, h_\xi=v_\xi} &\equiv M_3, \quad \frac{d^2V_0(h_\phi, h_\xi)}{dh_\phi dh_\xi} \Big|_{h_\phi=v_\phi, h_\xi=v_\xi} \equiv N_3, \\ \frac{d^2V_0(h_\phi, h_\xi)}{dh_\xi^2} \Big|_{h_\phi=v_\phi, h_\xi=v_\xi} &\equiv P_3. \end{aligned} \quad (14)$$

$$\begin{aligned} \frac{d^2V_T(h_\phi, h_\xi, T_{2C})}{dh_\phi^2} \Big|_{h_\phi=h_\phi^B, h_\xi=h_\xi^B} &\equiv M_5, \quad \frac{d^2V_T(h_\phi, h_\xi, T_{2C})}{dh_\phi dh_\xi} \Big|_{h_\phi=h_\phi^B, h_\xi=h_\xi^B} \equiv N_5, \\ \frac{d^2V_T(h_\phi, h_\xi, T_{2C})}{dh_\xi^2} \Big|_{h_\phi=h_\phi^B, h_\xi=h_\xi^B} &\equiv P_5, \end{aligned} \quad (15)$$

$$\begin{aligned} \frac{d^2V_T(h_\phi, h_\xi, T_{2C})}{dh_\phi^2} \Big|_{h_\phi=0, h_\xi=h_\xi^{2C}} &\equiv M_6, \quad \frac{d^2V_T(h_\phi, h_\xi, T_{2C})}{dh_\phi dh_\xi} \Big|_{h_\phi=0, h_\xi=h_\xi^{2C}} \equiv N_6, \\ \frac{d^2V_T(h_\phi, h_\xi, T_{2C})}{dh_\xi^2} \Big|_{h_\phi=0, h_\xi=h_\xi^{2C}} &\equiv P_6. \end{aligned} \quad (16)$$

Here, at finite temperature T_{2C} , the $h_{\phi, \xi}^B$ locates around $v_{\phi, \xi}$, and the h_ξ^{2C} locates around $h_{\xi_{C_{1(2)}}}$ as given in Eq. (2). That the temperature of the first step phase transition is higher than the second one, i.e., $T_{1C} > T_{2C}$, is also used to select the SFOEWPT points for the two step phase transition scenario.

At zero temperature, the $C_{1,2}$ can be a local minimum or saddle point with the global vacuum being located at B . We show in Fig. 3 how the phase transitions occur as the temperature drops in two-step case. During these two-step phase transition processes, the global vacuum of the finite temperature potential V_T changes from the A to the $C_{1,2}$ at the first-step after $T < T_{1C}$. Then, the phase changes from the vacuum locating around $C_{1,2}$ to the one around B , i.e., the EW symmetry breaking vacuum, after $T < T_{2C}$.

The above procedure is firstly used to obtain the critical phase transition order parameters and the rough phase transition pattern (either one-step or two-step). Subsequently, we use `CosmoTransitions` [25] to obtain the phase transition order parameters at the bubble nucleation temperature, which might be slightly different with the patterns from the above approach. This is mainly due to the reason that in some cases, although we can obtain the phase transition with the above approach, the improper barrier between the two minima at the bubble nucleation temperature couldn't fulfill the condition of bubble nucleation, see Eq. (36). This is especially important for the two-step cases where the pattern would be changed from $A \rightarrow C_{1,2} \rightarrow B$ to $A \rightarrow B$. Hence, when we present the results, the term ‘‘two-step’’ refers to the points obtained by the above approach, and the terms ‘‘bubble one-step’’ and ‘‘bubble two-step’’ refer to the points that can trigger one-step bubble nucleation and two-step bubble nucleation respectively after we check the bubble nucleation using `CosmoTransitions`.

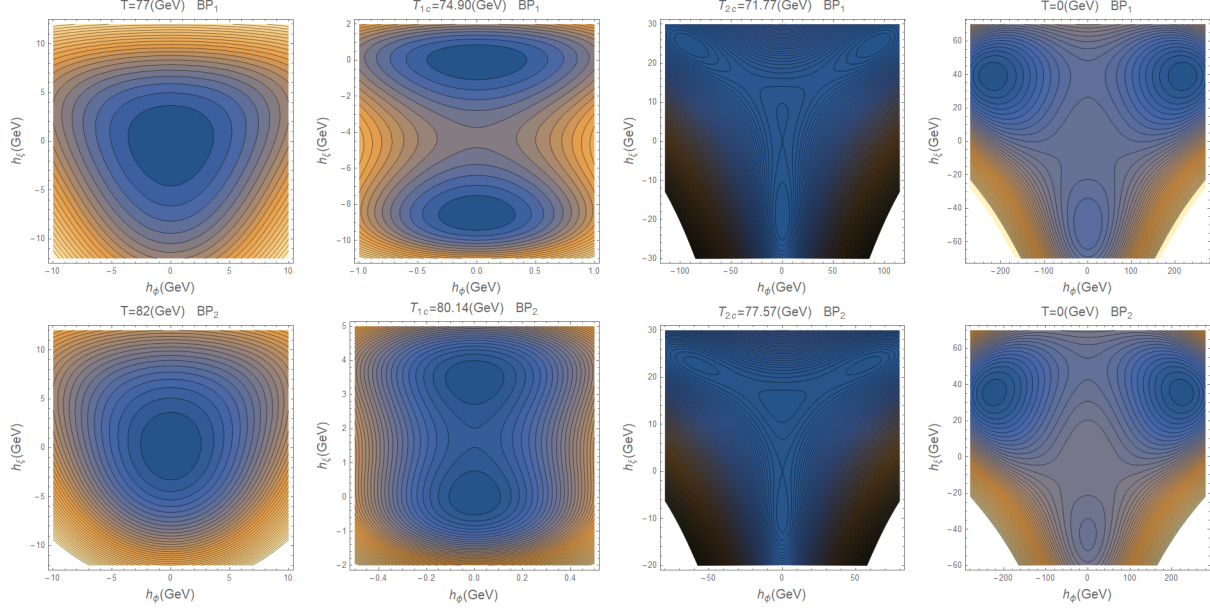


FIG. 3. The evolution of the vacuum structure as temperature drops. The two-step SFOEWPT point ($A \rightarrow C_2 \rightarrow B$) with the initial phase of the second step locating around C_2 for BP_1 . The two-step SFOEWPT point with the phase transition pattern of $A \rightarrow C_1 \rightarrow B$ and the initial phase of the second step locating around C_1 for BP_2 . The parameters for BP_1 are: $\lambda_1 = 0.040, \lambda_2 = 0.598, \lambda_3 = -0.113, \lambda_4 = 0.425, \lambda_5 = 0.264, \theta = 0.467, \mu_1 = -175.619 \text{ GeV}, \mu_2 = 14.416 \text{ GeV}$. The parameters for BP_2 are: $\lambda_1 = 0.039, \lambda_2 = 0.692, \lambda_3 = -0.311, \lambda_4 = 0.479, \lambda_5 = 0.457, \theta = 0.423, \mu_1 = -181.111 \text{ GeV}, \mu_2 = -6.144 \text{ GeV}$.

III. THE SFOEWPT AND HIGGS PHENOMENOLOGY

The vacuum structure at zero temperature, such as the potential barrier, is crucial for both one-step and two-step SFOEWPT. The desired vacuum structure for the SFOEWPT reveals the Higgs potential shape with triple and quartic Higgs couplings deviations from the SM case. The typical vacuum structure for one-step and two-step SFOEWPT being explored in the last section can have distinct Higgs phenomenological predictions.

In the GM model, both the two extra triplets contribute to the EWSB and the gauge bosons get masses also from the triplet VEV, $v_{\xi, \chi}$. The Electroweak charge of the triplets leads to the HVV couplings deviating from the singlet case by one extra factor $\sin \theta_H$, which parameterizes the contribution of the $v_{\xi, \chi}$ to the Higgs VEV, $\sin \theta_H = 2\sqrt{2}v_{\xi} / \sqrt{(8v_{\xi}^2 + v_{\phi}^2)}$ [26]. For the GM model, due to the isospin triplet contribute to the EWSB, the phase transition strength is defined

as [18],

$$\begin{aligned} v^{GM}/T &\equiv \frac{\sqrt{v_\phi^2(T) + 8v_\xi^2(T)}}{T} = \frac{v_\phi(T) \cos \theta_H(T)^{-1}}{T}, \\ \cos \theta_H(T) &\equiv \frac{v_\phi(T)}{\sqrt{v_\phi^2(T) + 8v_\xi^2(T)}}, \end{aligned} \quad (17)$$

at the critical temperature where phase transition occurs. Since we are working in the scenario where the zero temperature vacuum structure is crucial for the SFOEWPT, the $\theta_H(T)$ here would be highly related with the θ_H (see our previous studies in Ref [18] for detail). As will be explored latter, one can expect that the one-step and two-step SFOEWPT valid regions are highly restricted by collider searches.

To study the collider phenomenology of new physics models, one needs to work in the physical basis. In terms of physical field basis after taking into account of the rotation matrix (with the angle α) among classical fields and Higgs fields h, H , the interaction strength between the SM-like Higgs and SM particles are:

$$\begin{aligned} g_{h f \bar{f}} &= \cos \alpha / \cos \theta_H g_{h f \bar{f}}^{SM}, \quad g_{h V V} = (\cos \alpha \cos \theta_H - \sqrt{\frac{8}{3}} \sin \alpha \sin \theta_H) g_{h f \bar{f}}^{SM}, \\ g_{H f \bar{f}} &= \sin \alpha / \cos \theta_H g_{h f \bar{f}}^{SM}, \quad g_{H V V} = (\sin \alpha \cos \theta_H + \sqrt{\frac{8}{3}} \cos \alpha \sin \theta_H) g_{h f \bar{f}}^{SM}. \end{aligned} \quad (18)$$

Currently, the angle θ_H is severely bounded by the same-sign WW boson channel search at 13 TeV LHC [27]. Future hadron and lepton colliders would further restrict the magnitude of α and θ_H , which means that the possibility to reach SFOEWPT would be bounded to the parameter spaces with small $\sin \theta_H$ and small α . For the case of small θ_H limit where the EWSB contribution from the triplet is negligible, one will also have

$$\alpha \approx -\sqrt{\frac{3}{2}} \theta_H + \frac{\theta_H^2 (8\sqrt{3}\lambda_1 - 2\sqrt{3}\lambda_4 - \sqrt{3}\lambda_5) v}{\mu_1}. \quad (19)$$

This means, for a small θ_H one usually have a small α , and the sign of α is determined by the coupling combinations of $8\sqrt{3}\lambda_1 - 2\sqrt{3}\lambda_4 - \sqrt{3}\lambda_5$ and μ_1 . In the scenario with small α and small θ_H , the $g_{h f \bar{f}}, g_{H V V}$ close to the SM case, $g_{H f \bar{f}}, g_{H V V}$ are suppressed.

The scalar potential of Eq. (1) in the Higgs basis of h and H can be written as,

$$\begin{aligned} V_{phy}^{GM} &= \frac{1}{2} m_1^2 (h \cos \alpha + H \sin \alpha)^2 + \frac{1}{2} m_2^2 (H \cos \alpha - h \sin \alpha)^2 \\ &+ \frac{2}{\sqrt{3}} \mu_2 (H \cos \alpha - h \sin \alpha)^3 + \frac{\sqrt{3}}{4} \mu_1 (h \cos \alpha + H \sin \alpha)^2 (H \cos \alpha - h \sin \alpha) \\ &+ \lambda_1 (h \cos \alpha + H \sin \alpha)^4 + (\lambda_2 + \frac{1}{3} \lambda_3) (H \cos \alpha - h \sin \alpha)^4 \\ &+ (\lambda_4 + \frac{1}{2} \lambda_5) (h \cos \alpha + H \sin \alpha)^2 (H \cos \alpha - h \sin \alpha)^2, \end{aligned} \quad (20)$$

for the GM model. In the small α limit, the potential V_{phy}^{GM} reduces to

$$\begin{aligned} V_{\alpha}^{GM} = & \frac{1}{2}m_1^2 h^2 + \lambda_1 h^4 + \frac{1}{2}m_2^2 H^2 + \frac{2\sqrt{3}}{3}\mu_2 H^3 + \frac{1}{3}(3\lambda_2 + \lambda_3)H^4 + \frac{\sqrt{3}}{4}\mu_1 h^2 H \\ & + \frac{1}{2}(2\lambda_4 + \lambda_5)h^2 H^2 + \alpha h \left(-\frac{\sqrt{3}\mu_1}{4}h^2 + (m_1^2 - m_2^2)H + \frac{\sqrt{3}}{2}(\mu_1 - 4\mu_2)H^2 \right. \\ & \left. + (-4\lambda_2 - \frac{4\lambda_3}{3} + 2\lambda_4 + \lambda_5)H^3 + (4\lambda_1 - 2\lambda_4 - \lambda_5)h^2 H \right) + \mathcal{O}(\alpha^2). \end{aligned} \quad (21)$$

After EWSB, h and H get VEVs,

$$\begin{aligned} v_h^{GM} &= v \cos(\alpha) \cos(\theta_H) - \frac{1}{2}\sqrt{\frac{3}{2}}v \sin(\alpha) \sin(\theta_H), \\ v_H^{GM} &= v \sin(\alpha) \cos(\theta_H) + \frac{1}{2}\sqrt{\frac{3}{2}}v \cos(\alpha) \sin(\theta_H), \end{aligned} \quad (22)$$

with $v = v_{SM} \equiv 246$ GeV, and $v_{\xi} = v \sin \theta_H / 2\sqrt{2}$. Suppose h is the SM-like Higgs, one has both the Higgs cubic and quartic couplings being modified comparing with the SM case. This can be parameterized as:

$$\Delta\mathcal{L} = -\frac{1}{2}\frac{m_h^2}{v}(1 + \delta\kappa_3)h^3 - \frac{1}{8}\frac{m_h^2}{v^2}(1 + \delta\kappa_4)h^4, \quad (23)$$

The cubic Higgs couplings are crucial for the vacuum structure and therefore the phase transition dynamics, as well as the Higgs pair production at hadron and lepton colliders. Consequently, the Higgs pair searches could be powerful to probe the parameter space of the SFOEWPT. In the small α (θ_H) limit, we have

$$\delta\kappa_3^{GM} = -\alpha \frac{\sqrt{3}\mu_1 v}{2m_h^2} + \frac{\alpha v^2(4\alpha - \sqrt{6}\theta_H)(2\lambda_4 + \lambda_5)}{2m_h^2} - \frac{(3\alpha^2 + \theta_H^2)}{2} + \mathcal{O}(\alpha^3, \theta_H^3), \quad (24)$$

$$\delta\kappa_4^{GM} = -2\alpha^2 \left(1 - \frac{2(2\lambda_4 + \lambda_5)v^2}{m_h^2} \right) + \mathcal{O}(\alpha^3). \quad (25)$$

As a comparison, we also list the case for xSM model which has no extra EWSB contribution. In xSM case, we also define a mixing angle α between the SM Higgs (h) and extra scalar (s). At the zero temperature, it is defined as [28]

$$\sin 2\alpha = \frac{(a_1 + 2a_2 v_s)v_h}{(m_h^2 - m_H^2)}, \quad (26)$$

with $v_h = 246$ GeV. For $-1 \leq \sin 2\alpha \leq 1$, which sets a bound on the VEV fraction of the SM Higgs (h),

$$m_h^2 - m_H^2 \leq (a_1 + 2a_2 v_s)v_h \leq m_H^2 - m_h^2. \quad (27)$$

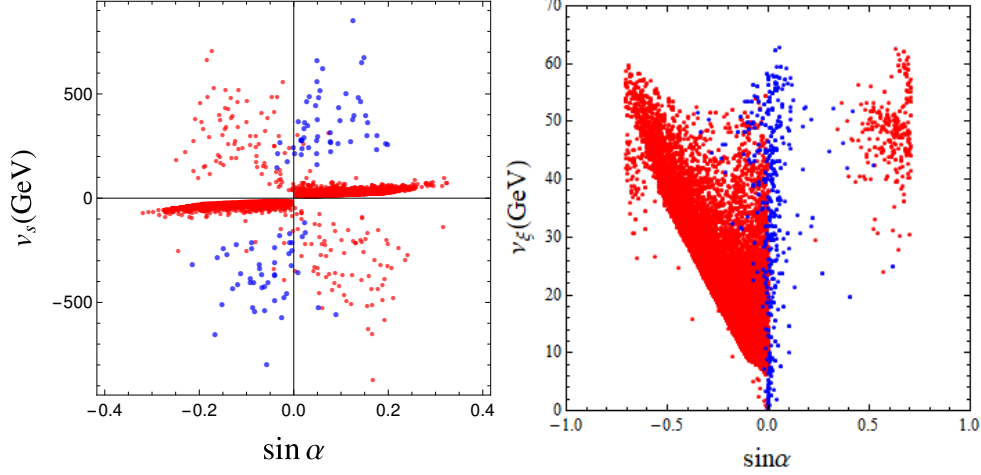


FIG. 4. The $v_C/T_C > 1$ viable points (both one-step (red) and two-step (blue)) in the $\sin \alpha$ - $v_{s,\xi}$ plane for the xSM (left) and the GM (right) model.

The phase transition occurs in the subspace of the two scalar fields, with the phase transition strength being

$$v^{\text{xSM}}/T \equiv \frac{v_h(T)}{T} = \frac{\sqrt{v_h^2(T) + v_s^2(T)} \cos \theta(T)}{T},$$

$$\cos \theta(T) \equiv \frac{v_h(T)}{\sqrt{v_h^2(T) + v_s^2(T)}}. \quad (28)$$

The sphaleron process is quenched when $v_h(T)/T > 1$ at the critical temperature. Different from the GM model, the singlet VEV (v_s) does not contribute to the mass of gauge boson due to the Electroweak charge of the singlet, hence it does not contribute to the phase transition strength.

The collider search of the Higgs phenomenology is performed in the basis of the SM Higgs and one extra heavy Higgs. The current LHC Higgs data and theoretical constraints require small α which parameterizes the mixing between the SM-like Higgs and the extra CP-even heavy Higgs. In this model, all the couplings are rescaled by α based on the SM as: $g_{hxx} = \cos \alpha g_{hxx}^{\text{SM}}$, $g_{Hxx} = -\sin \alpha g_{hxx}^{\text{SM}}$. Therefore, no direct bound on the angle $\theta(T=0)$ from the Higgs data since the parameter does not enter Higgs couplings. The VEV of the extra scalar (v_s) would be more free than that in GM model.

For the xSM model, the potential in the basis of Higgs fields is given by,

$$V_{\text{phy}}^{\text{xSM}} = \frac{1}{12} (3a_1(h \cos \alpha - H \sin \alpha)^2(h \sin \alpha + H \cos \alpha) + 3a_2(h \cos \alpha - H \sin \alpha)^2 \\ \times (h \sin \alpha + H \cos \alpha)^2 + 6b_2(h \sin \alpha + H \cos \alpha)^2 + 4b_3(h \sin \alpha + H \cos \alpha)^3 \\ + 3b_4(h \sin \alpha + H \cos \alpha)^4 + 3\lambda(h \cos \alpha - H \sin \alpha)^4 - 6\mu^2(h \cos \alpha - H \sin \alpha)^2). \quad (29)$$

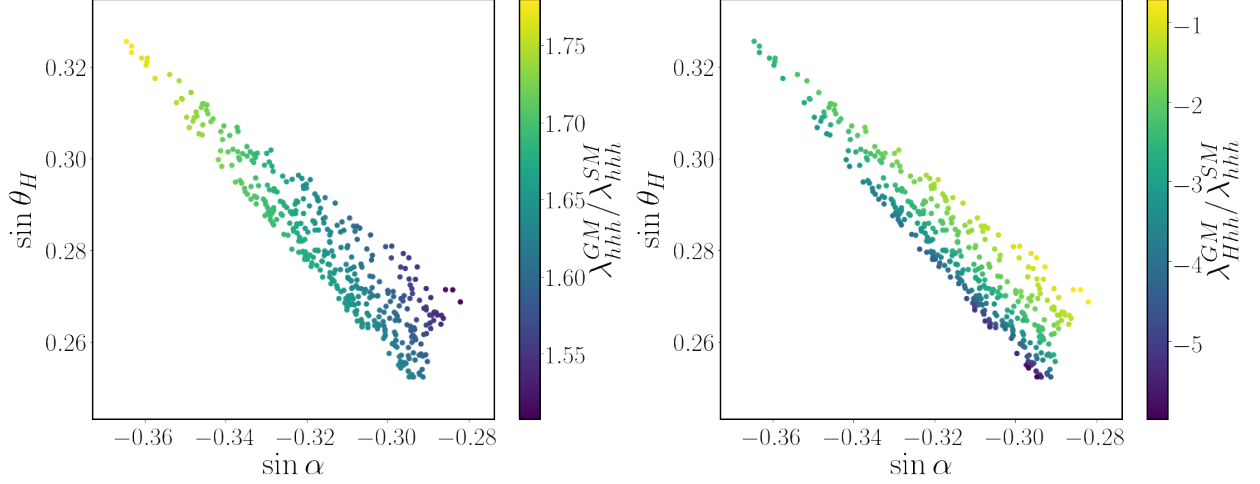


FIG. 5. The ratio of $\lambda_{hhh}^{GM}/\lambda_{hhh}^{SM}$ (left) and $\lambda_{Hhh}^{GM}/\lambda_{hhh}^{SM}$ (right) in $\sin\alpha$ - $\sin\theta_H$ plane in $H5$ plane.

Going to the alignment case, one have,

$$\begin{aligned}
 V_\alpha^{\text{xSM}} = & \frac{1}{12}(3a_1h^2H + 3a_2h^2H^2 + 6b_2H^2 + 4b_3H^3 + 3b_4H^4 + 3h^4\lambda - 6h^2\mu^2) \\
 & + \frac{1}{4}h\alpha(a_1(h^2 - 2H^2) + 2H(a_2(h^2 - H^2) + 2b_2 + 2(H(b_3 + b_4H) - \lambda h^2 + \mu^2))) \\
 & + \mathcal{O}(\alpha^2) .
 \end{aligned} \tag{30}$$

After EWSB, one have for the two physical fields h and H :

$$\begin{aligned}
 v_h^{\text{xSM}} &= v_h \cos(\alpha) + v_s \sin(\alpha) , \\
 v_H^{\text{xSM}} &= v_s \cos(\alpha) - v_h \sin(\alpha) .
 \end{aligned} \tag{31}$$

In the xSM, the deviation of the cubic and quartic couplings for small α are given by [29]:

$$\begin{aligned}
 \delta\kappa_3^{\text{xSM}} &= \alpha^2 \left[-\frac{3}{2} + \frac{2m_H^2 - 2b_3v_s - 4b_4v_s^2}{m_h^2} \right] + \mathcal{O}(\alpha^3) , \\
 \delta\kappa_4^{\text{xSM}} &= \alpha^2 \left[-3 + \frac{5m_H^2 - 4b_3v_s - 8b_4v_s^2}{m_h^2} \right] + \mathcal{O}(\alpha^3) .
 \end{aligned} \tag{32}$$

Due to the extra EWSB contribution, in the GM model, one has an additional angle θ_H to parameterize the Higgs couplings. Therefore one has the different distributions of SFOEWPT points in the v_ξ - α plane, which builds the bridge between the SFOEWPT and the Higgs phenomenology. Fig. 4 shows the one-step (red) and two-step (blue) SFOEWPT valid points in the xSM (left) and GM (right) model. For the xSM case, the one-step (two-step) SFOEWPT points concentrate in the small (large) v_s regions. While in the GM model, the v_ξ is much smaller than the v_s in xSM and the possibility to reach a SFOEWPT drops with the decrease of the v_ξ and $|\sin\alpha|$.

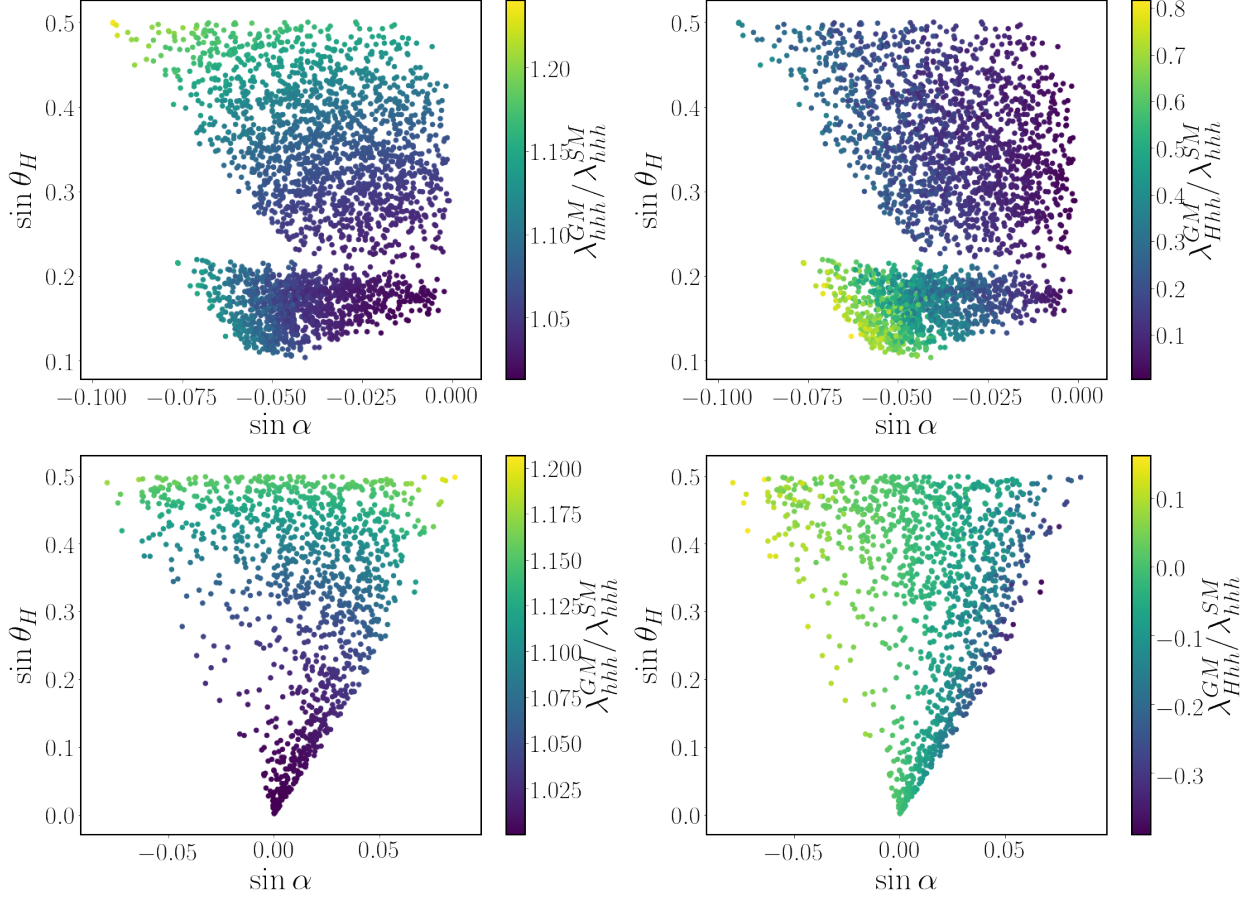


FIG. 6. The ratio of $\lambda_{hhh}^{GM} / \lambda_{hhh}^{SM}$ (left panels) and $\lambda_{Hhh}^{GM} / \lambda_{hhh}^{SM}$ (right panels) in $\sin \alpha$ - $\sin \theta_H$ plane for both one-step points (upper panels) and two-step points (lower panels) in *low mass benchmark*.

In the parameter spaces which allow the SFOEWPT, one has the deviations of the cubic and quartic Higgs couplings, which characterize the Higgs potential shape that are crucial for the realization of the EWSB mechanism. We investigate more details in two particular benchmarks of the GM model: the *H5plane* which is developed by the LHC Higgs Cross Section Working Group for fiveplet searches [30] and the *low mass benchmark* studied in [31] for lower mass region. Both benchmark scenarios will lead to interesting searches at the collider.

Our previous study in [18] shows that, only one-step SFOEWPT is valid in *H5plane*, while the *low mass benchmark* can provide both one-step and two-step SFOEWPT. After considering the current LHC search bounds, especially the same-sign W search from CMS [27], we show the triple scalar couplings in Fig. 5 and Fig. 6 for *H5plane* and *low mass benchmark* respectively. In *H5plane*, Fig. 5 shows that a larger deviation of the triple Higgs coupling λ_{hhh}^{GM} from the SM one occurs with a higher magnitude of $|\alpha|$ and a larger θ_H . While the λ_{Hhh}^{GM} is highly enhanced with an extra sign compared with g_{hhh}^{SM} which can result in destructive interference for Higgs pair production at the collider.

In *low mass benchmark*, one has smaller $\sin \theta_H$ and m_{h_5} in comparison with the *H5plane* scenario. The CMS same-sign W search severely bounds the $\sin \theta_H$ and thus the mixing angle α . Therefore one can expect the triple Higgs coupling and the quartic Higgs couplings are all restricted. In Fig. 6, we show the triple Higgs couplings in $\sin \alpha$ - $\sin \theta_H$ plane for both one (upper panels) and two-step (lower panels) SFOEWPT. The SFOEWPT viable points in *low mass benchmark* locate in smaller value of θ_H and α . Thus we have lower enhancement in λ_{hhh}^{GM} than that in *H5plane*. Meanwhile, the λ_{Hhh}^{GM} is also much more smaller than that in *H5plane*. These will result in different gravitational wave production and collider phenomenology as we will study in the following.

A SFOEWPT can also be reached with the help of the dimensional six operator $(H^\dagger H)^3$ [32, 33] or new physics that can contribute to such operator. The collider couldn't tell the detailed potential shape (i.e., the tree level potential barrier) that drives the phase transition. In this case, the gravitational wave search for the signal generated by the SFOEWPT would be complementary, since it captures the tunneling process manifested in terms of the vacuum bubble nucleations [7].

IV. GRAVITATIONAL WAVE SEARCHES

When the temperature of the Universe further cools down after the critical temperature T_C (where one has the degeneracy of the true and the false vacuum), one may have vacuum bubble nucleations, expansions and collisions, and therefore generate GW signals from the SFOEWPT process.

The bounce configuration of the nucleation bubble (the bounce configuration of the multi-fields that connects the EW broken vacuum (h -vacuum, the true vacuum locate around B point) and the false vacuum (the vacuum locate around A or C points)) can be obtained by extremizing

$$S_3(T) = \int 4\pi r^2 dr \left[\frac{1}{2} \left(\frac{d\phi_b}{dr} \right)^2 + V(\phi_b, T) \right], \quad (33)$$

through solving the equation of motion for ϕ_b (it is h and h_ξ for two-step scenarios),

$$\frac{d^2 \phi_b}{dr^2} + \frac{2}{r} \frac{d\phi_b}{dr} - \frac{\partial V(\phi_b)}{\partial \phi_b} = 0, \quad (34)$$

with the boundary conditions of

$$\lim_{r \rightarrow \infty} \phi_b = 0, \quad \frac{d\phi_b}{dr} \Big|_{r=0} = 0. \quad (35)$$

The phase transition completes at the nucleation temperature when the thermal tunnelling probability for bubble nucleation per horizon volume and per horizon time is of order unity [34–36]:

$$\Gamma \approx A(T) e^{-S_3/T} \sim 1. \quad (36)$$

One of the crucial parameter for the gravitational wave is α , which is the energy budget of SFOEWPT normalized by the radiative energy, defined as

$$\alpha = \frac{\Delta \rho}{\rho_R}, \quad (37)$$

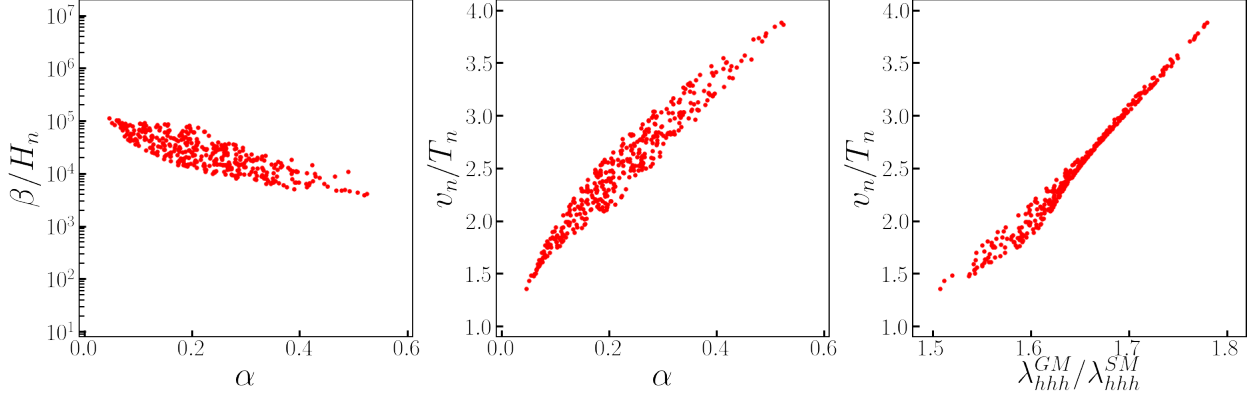


FIG. 7. The scanned results in α - β/H_n (left), α - v_n/T_n (middle) and $\lambda_{hhh}^{GM}/\lambda_{hhh}^{SM}$ - v_n/T_n (right) planes for *H5plane* where we have only one-step (red) points.

where the radiation energy of the bath or the plasma background ρ_R is given by

$$\rho_R = \frac{\pi^2 g_\star T_\star^4}{30}, \quad (38)$$

The parameter $\Delta\rho$ is the latent heat (vacuum energy density or energy budget of SFOEWPT) from the phase transition to the energy density of the radiation bath or the plasma background. This is given by the difference of the energy density between the false (here it is ϕ vacuum, $\rho(\phi_n, T)$) and the true vacuum (the h -vacuum or EW broken vacuum, $\rho(v_n, T)$),

$$\rho(\phi_n, T_n) = -V(\phi, T)|_{T=T_n} + T \frac{dV(\phi, T)}{dT}|_{T=T_n}, \quad (39)$$

$$\rho(v_n, T_n) = -V(h, T)|_{T=T_n} + T \frac{dV(h, T)}{dT}|_{T=T_n}. \quad (40)$$

Another crucial parameter β characterizes the inverse time duration of the SFOEWPT and thus the GW spectrum peak frequency is defined as

$$\frac{\beta}{H_n} = T \frac{d(S_3(T)/T)}{dT}|_{T=T_n}, \quad (41)$$

with H_n being the Hubble constant at the bubble nucleation temperature T_n .

Considering all the constraints from the LHC, especially the same-sign W bounds from CMS [27], we show the results in Fig. 7 and Fig. 8 for *H5plane* and *low mass benchmark* respectively, where the red points represent the one-step scenario and the blue points represent the two-step case. As mentioned before, we separate the two-step points into two groups according to the scan results from *CosmoTransition*. The dark blue circle points represent the case where we have two-step bubble nucleation (“bubble two-step”), while the light blue triangle points are those we have only one bubble nucleation (“bubble one-step”).

In either *H5plane* or *low mass benchmark* (one-step and two-step), the β/H_n decreases with the increase of α . While α is also found to be proportional to the phase transition strength v_n/T_n ,

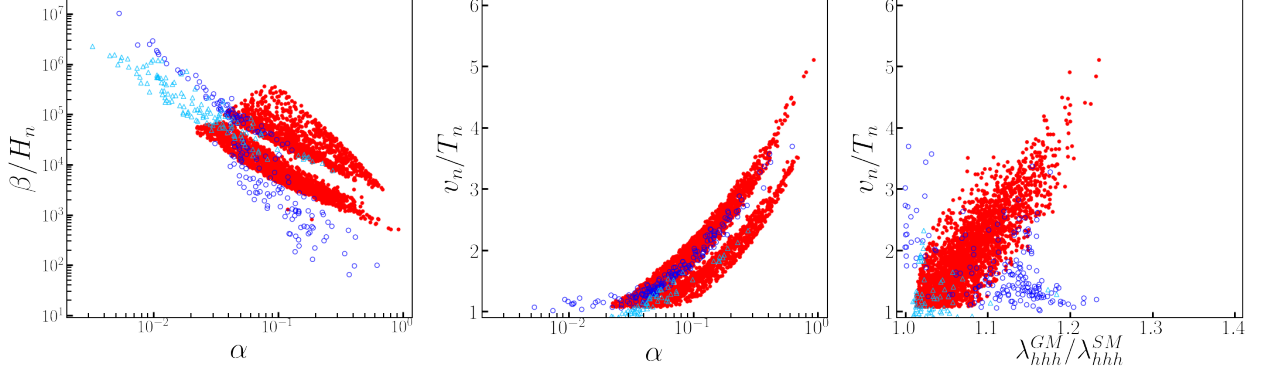


FIG. 8. The scanned results in α - β/H_n (left), α - v_n/T_n (middle) and $\lambda_{hhh}^{GM}/\lambda_{hhh}^{SM}$ - v_n/T_n (right) planes for *low mass benchmark* where we have both one-step (red) and two-step (blue) points. Among the blue points, the circle points represent the case where we can have two-step bubble nucleation (“bubble two-step”), while the triangle points are those where we have only one bubble nucleation (“bubble one-step”).

larger value of α is obtained at larger value of v_n/T_n which results in a relatively larger energy density of the gravitational wave spectrum. As a comparison, beside that the triple/quartic scalar coupling is smaller in the *low mass benchmark*, the *low mass benchmark* also provides lower β/H_n in the similar range of α than that in *H5plane*, which is necessary to produce detectable gravitational wave. In *low mass benchmark* where we have both one-step and two-step scenarios, two-step SFOEWPT will have relatively smaller β/H_n and larger v_n/T_n for the same α than one-step scenario.

Here the most stringent constraint comes from the CMS same-sign diboson search [27] which, however, doesn’t extend to mass (m_5) below 200 GeV. This is not relevant for *H5plane*, since all those points in Fig. 7 have $m_5 > 200$ GeV. However, in *low mass benchmark*, we can clearly see two parts of points for one-step scenario in Fig. 8². Those with lower β/H_n or larger v_n/T_n , hence resulting in more detectable GW signal, are the points having mass below 200 GeV, which require more dedicated searches at collider. The triple Higgs couplings are also shown with respect to the SM scenario. The triple Higgs coupling is proportional to phase transition strength v_n/T_n for one-step points in both *H5plane* and *low mass benchmark*, while there is no clear relation for the two-step points in *low mass benchmark*.

At last, we comment on the situation in xSM. In Fig. 9, we show the relation among β/H_n , α , v_n/T_n and triple scalar couplings in xSM³. Since the singlet VEV v_s has no restrictions in general in xSM, the magnitude of β/H_n (v_n/T_n and α) is relatively much lower (larger) than that in GM model, which results in more detectable GW signal, while the triple scalar couplings has similar enhancement as in GM model.

² We do have two parts for two-step as well. However, the points with mass above 200 GeV is minority, we don’t discuss them separately.

³ In this and the following plots for the xSM, we use the same set of data points as used in Ref. [29].

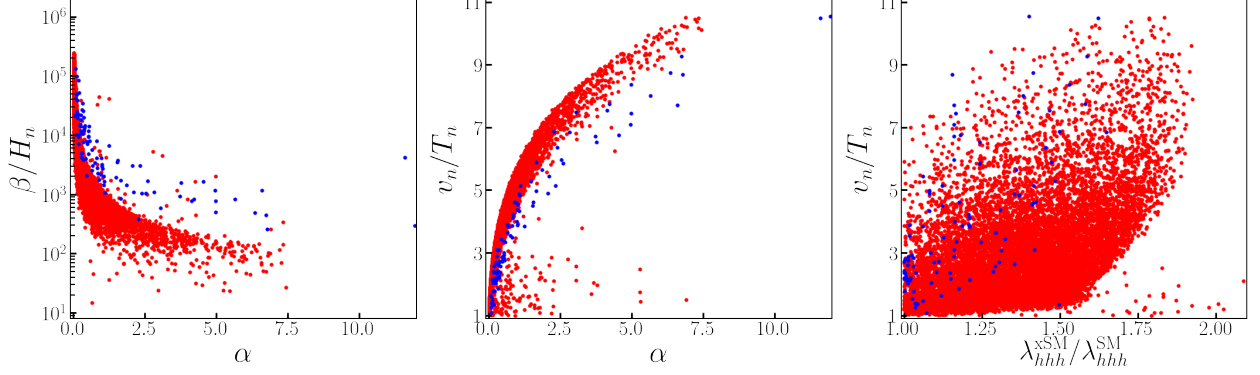


FIG. 9. SFOEWPT valid points in α - β/H_n (left), α - v_n/T_n (middle) and $\lambda_{hhh}^{xSM}/\lambda_{hhh}^{SM}$ - v_n/T_n (right) planes for xSM. Red and blue points represent one and two-step scenario respectively.

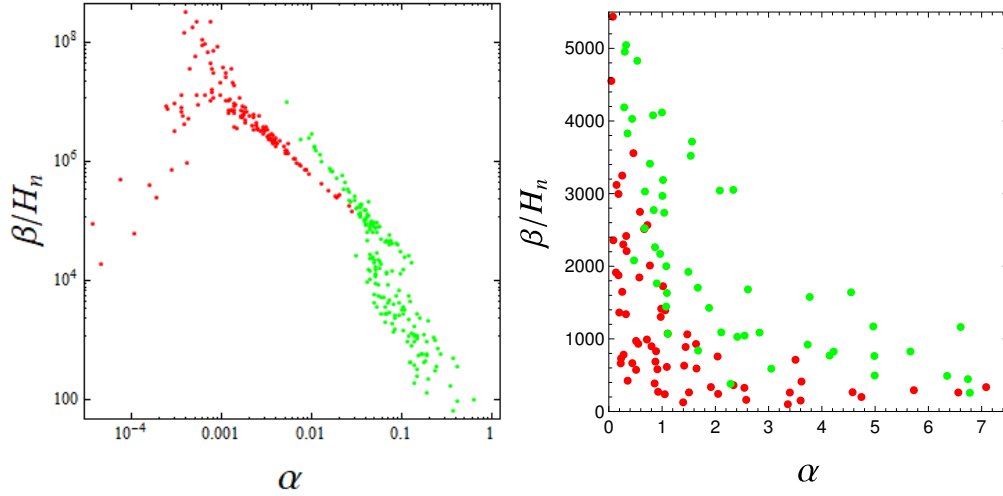


FIG. 10. The GW signal parameters for the case with extra EWSB (GM) and without EWSB (xSM). The red and green points correspond to the first and the second step of the two-step SFOEWPT.

In Fig. 10, we show the two crucial parameters for the GW signals. The left panel indicates the scenario with EWSB contribution. Due to the extra EWSB contribution is subject to severely bounds from the LHC, the extra VEV is small. Which limit the vacuum structure that is important for the phase transition, and thus the first step phase transition can be weakly first order and the GW signal being generated are negligible (with a small α and large β/H_n), the GW signals in this case mostly dominated by the second-step SFOEWPT which characterize the dynamical EWSB. The right panel is shown here for comparison, one may find that the α and β/H_n of the first-step phase transition is mostly smaller than the second-step, which imply a GW signal mostly come from the first-step which does not characterize any symmetry breaking, see Ref. [29] for details.

There are mainly two sources for GW production during the EWPT: the sound waves in the plasma [37, 38] and the magnetohydrodynamic turbulence (MHD) [37, 38] while the contribution from bubble wall collisions [39–44] are now generally believed to be negligible [45]. The energy density spectrum from the sound waves can be well expressed by [38]

$$\Omega_{\text{sw}} h^2 = 2.65 \times 10^{-6} \left(\frac{H_*}{\beta} \right) \left(\frac{\kappa_v \alpha}{1 + \alpha} \right)^2 \left(\frac{100}{g_*} \right)^{1/3} v_w \left(\frac{f}{f_{\text{sw}}} \right)^3 \left(\frac{7}{4 + 3(f/f_{\text{sw}})^2} \right)^{7/2}. \quad (42)$$

where H_* is the Hubble parameter at the temperature T_* , at the time when the EWPT finishes; v_w is the bubble wall velocity; α is the energy released from the EWPT normalized by the total radiation energy density at T_* as mentioned above; g_* is the corresponding relativistic degrees of freedom making up the radiation energy density; β characterizes roughly the inverse time duration of the EWPT. Practically, T_* is very close to T_n and we use T_n in the following calculations. Moreover κ_v is the fraction of released energy going to the kinetic energy of the plasma, which can be calculated given v_w ⁴ and α [47]. Finally f_{sw} is the peak frequency of above energy density spectrum:

$$f_{\text{sw}} = 1.9 \times 10^{-5} \frac{1}{v_w} \left(\frac{\beta}{H_*} \right) \left(\frac{T_*}{100 \text{ GeV}} \right) \left(\frac{g_*}{100} \right)^{1/6} \text{ Hz}, \quad (43)$$

A small fraction of the energy goes to the MHD, whose contribution to the energy density spectrum can also be expressed as [48, 49]

$$\Omega_{\text{turb}} h^2 = 3.35 \times 10^{-4} \left(\frac{H_*}{\beta} \right) \left(\frac{\kappa_{\text{turb}} \alpha}{1 + \alpha} \right)^{3/2} \left(\frac{100}{g_*} \right)^{1/3} v_w \frac{(f/f_{\text{turb}})^3}{[1 + (f/f_{\text{turb}})]^{11/3} (1 + 8\pi f/h_*)}, \quad (44)$$

where κ_{turb} is the fraction of energy going to the MHD and following previous analyses, we take here $\kappa_{\text{turb}} \approx 0.1 \kappa_v$. Similar to f_{sw} , f_{turb} is the peak frequency for the spectrum from MHD:

$$f_{\text{turb}} = 2.7 \times 10^{-5} \frac{1}{v_w} \left(\frac{\beta}{H_*} \right) \left(\frac{T_*}{100 \text{ GeV}} \right) \left(\frac{g_*}{100} \right)^{1/6} \text{ Hz}. \quad (45)$$

In Fig. 11, we show the GW signal spectrum predicted in *H5plane* (left) and *low mass benchmark* (right) after considering the same-sign diboson bounds from CMS for several representative points taken from the tail of Fig. 7 and Fig. 8 (which are the most promising points for GW detection). In comparison with the *H5plane*, the GW signals from the SFOEWPT points of *low mass benchmark* can be more easy to be probed with a lower frequency.

With the GW spectrum obtained for each set of parameters input, the GW signals can be searched for using the cross correlation between the outputs of a pair of detectors. The detectability of the signals is quantified by the signal-to-noise ratio (SNR) [50]:

$$\text{SNR} = \sqrt{\mathcal{T} \int df \left[\frac{h^2 \Omega_{\text{GW}}(f)}{h^2 \Omega_{\text{exp}}(f)} \right]^2}, \quad (46)$$

where \mathcal{T} is the mission duration and Ω_{exp} is the power spectral density of a given detector.

⁴ A significant GW production usually needs a very relativistic value of the v_w , which however is dangerous for baryon asymmetry generation. To deal with this conundrum, we follow Ref. [7, 29, 46] by taking the plasma hydrodynamics into account and distinguish between v_w and the velocity used in baryogenesis calculations. Therefore a supersonic v_w can be realized while still maintaining a subsonic plasma velocity outside the bubble wall in the wall frame.

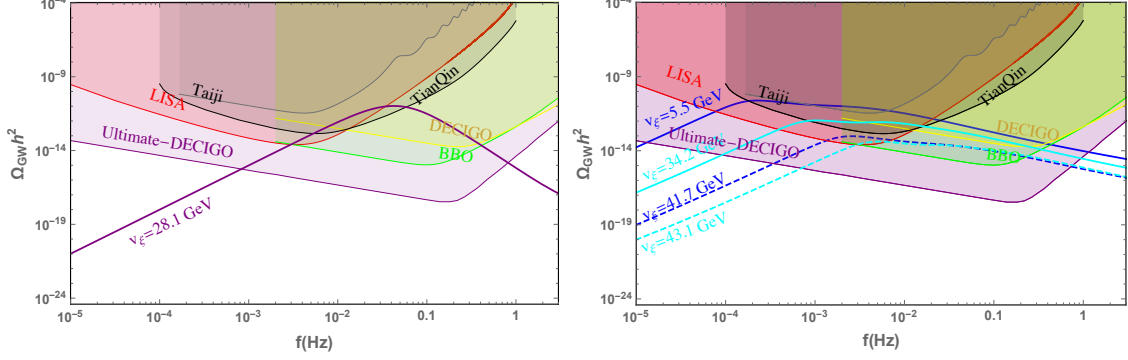


FIG. 11. The representative GW signal spectra for *H5plane* (left) and *low mass benchmark* (right). In *H5plane*, only one-step SFOEWPT (purple) is available, while in *low mass benchmark*, both one-step (cyan) and two-step (blue) are available. The corresponding value of v_ξ for each spectrum is also shown along each line.

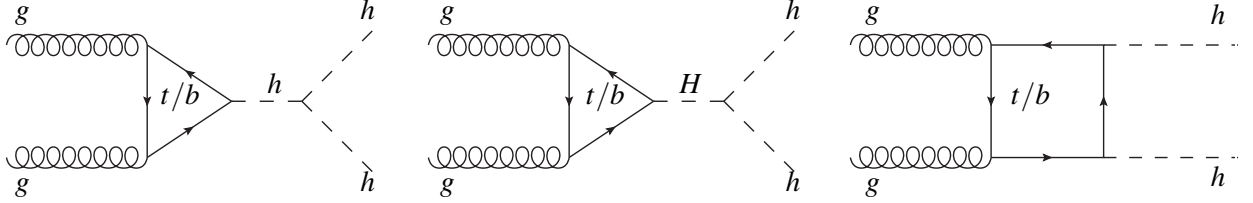


FIG. 12. The Feynman diagrams for the Higgs pair production with extra scalar at the LHC.

V. COLLIDER SEARCHES

From previous studies (e.g. Fig. 9 of Ref. [18]), we find that one-step and two-step phase transition would happen in different parameter space. In the *low mass benchmark*, current constraints from same-sign diboson searches already separated the one-step and two-step phase transition into two almost non-overlapping parts with two-step points preferring lower mass while one-step with higher mass. Further, the phase transition strength has a correlation with the triple Higgs coupling in the one-step case, while it is not necessary in the two-step case to have larger triple Higgs coupling to trigger the SFOEWPT.

On the other hand, the collider searches of the Higgs potential also concentrate on the triple Higgs couplings search: Higgs pairs search at hadron collider (LHC, HL-LHC, SppC, FCC-hh, etc.), Zhh production at lepton colliders (ILC, CEPC, FCC-ee, etc.). Further, the quartic Higgs coupling also enters Higgs pair production through either two-loop [51] or one-loop [52] contributions for hadron and lepton collider respectively. Hence the Higgs pair production searches will be nice places to further search these two cases at either the LHC or future lepton colliders.

The leading order contributions for Higgs pair production come from the one-loop diagrams shown in Fig. 12 with non-resonant and possible resonant productions. The non-resonant productions involve the box diagrams (right panel) and also triangle diagram (left panel) which de-

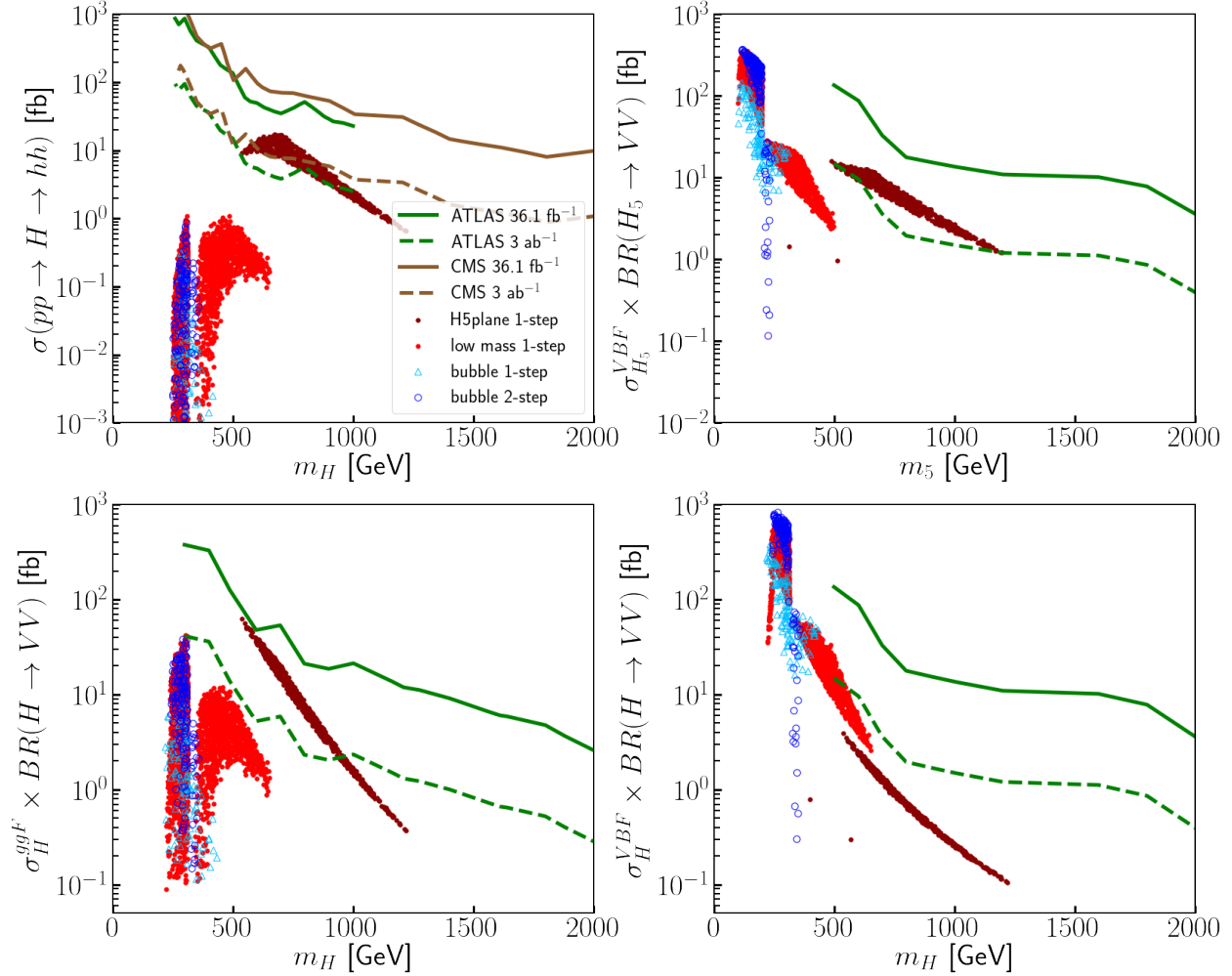


FIG. 13. The current and prospective di-Higgs and di-boson searches at the LHC for GM model in the H5plane (dark red for one-step) and low mass benchmark (red and blue for one-step and two-step respectively). The blue points are further separated into two categories: “bubble one-step” (light blue triangle) and “bubble two-step” (dark blue circle).

depends on the triple scalar coupling λ_{hhh} . While the resonant production involve the production of extra scalar and subsequent decays into Higgs pair which depends on the triple scalar coupling λ_{Hhh} . The differential cross section for the Higgs pair production have been carried out previously [53, 54]. The calculations have been implemented into MadGraph for several different cases [55]. For the GM model, we use the NLO UFO model files [56] implemented with FeynRules [57, 58] with MadGraph [59] to directly calculate the cross section for relevant processes. The required parameter cards are generated using GmCalc 1.4.1 [60]. Relevant work can also be found in [61].

The Higgs pair production cross section in the GM model are shown in the upper-left panels of Fig. 13 for *H5plane* and *low mass benchmark*. All points shown in these plots have passed

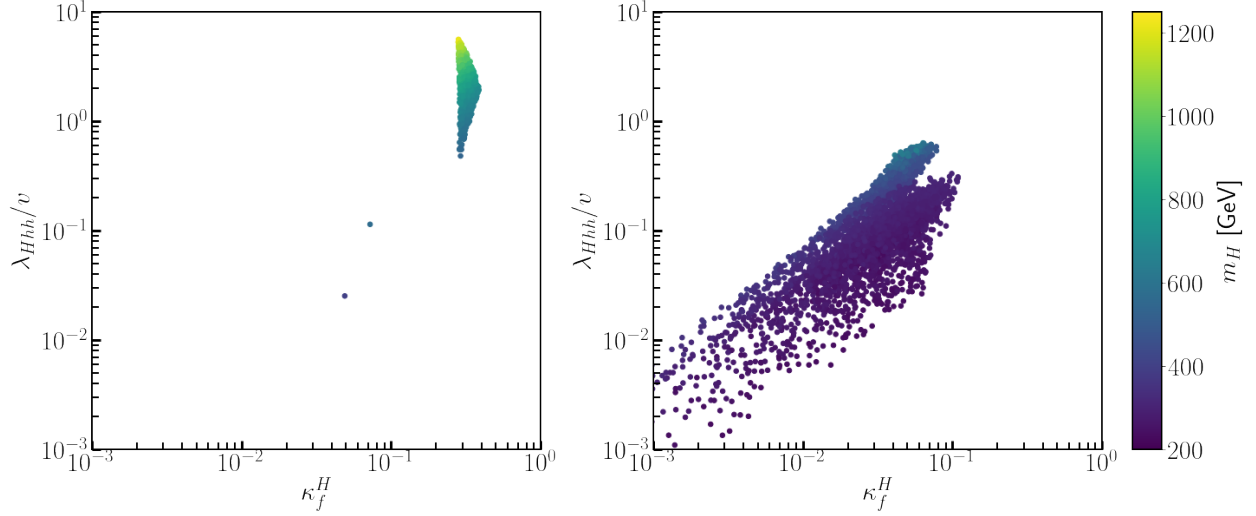


FIG. 14. SFOEWPT viable points in κ_f^H - λ_{Hhh} plane for $H5$ -plane (left) and low mass benchmark (right). The colors of the points represent the mass of H .

the CMS same-sign diboson searches [18, 27]. For $H5$ plane, only one-step phase transition exist (dark red points), while both one-step (red points) and two-step (blue points) phase transition can happen for *low mass benchmark*. For the two-step points (blue points) in *low mass benchmark*, we also separate them into two categories: “bubble one-step” and “bubble two-step”, the same as those in Fig. 8. In either case, current Higgs pair searches do not have sufficient sensitivity to probe the phase transition viable parameter space. However, with accumulated data from HL-LHC, it is possible to cover most points in $H5$ plane. While, points in *low mass benchmark* are still beyond the Higgs pair production measurements.

This can be understood from Fig. 14 in which we show the same points in λ_{Hhh} -BR($H \rightarrow hh$) plane for $H5$ plane (left panel) and *low mass benchmark* (right panel). It is clear that in $H5$ plane, which only has viable one-step points, the triple scalar coupling λ_{Hhh} is much larger than those in *low mass benchmark*. Hence, the branching of $H \rightarrow hh$ will be larger in $H5$ plane. On the other hand, the $\kappa_f^H \equiv \frac{g_{Hff}^{GM}}{g_{hff}^{SM}} = \frac{\sin \alpha}{\cos \theta_H}$, which contributes to the gluon-gluon fusion cross section, is also larger in $H5$ plane than that in *low mass benchmark*. As a consequence, the cross section of the resonance Higgs pair production is larger in $H5$ plane.

Beside the Higgs pair measurement, the diboson resonance searches will also have the sensitivity to probe the phase transition viable parameter space. Hence, in both $H5$ plane as well as *low mass benchmark*, we check the resonance diboson cross section through either H (gluon-gluon Fusion and VBF) or H_5 (VBF) against the experimental limits. The results are shown in the other three panels in Fig. 13. From these plots, we find that, $H5$ plane can be fully covered by the diboson searches from H_5 (VBF) and H (ggF) resonance production. While, *low mass benchmark* can still escape the searches. However, due to the large κ_V^H compared with κ_f^H , the VBF production of H is not highly suppressed, extending the relevant searches into lower mass region (below 500 GeV) will tremendously improve the sensitivity for such case.

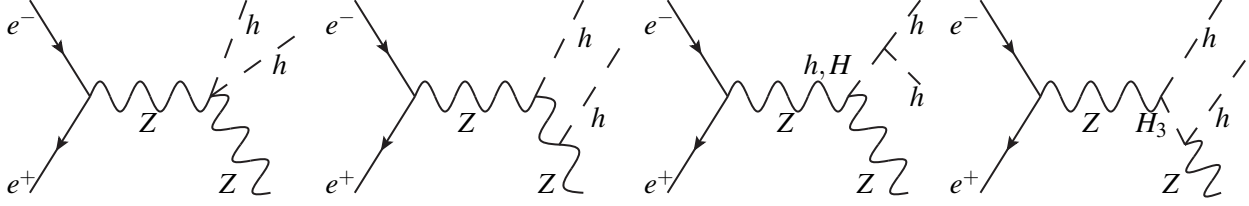
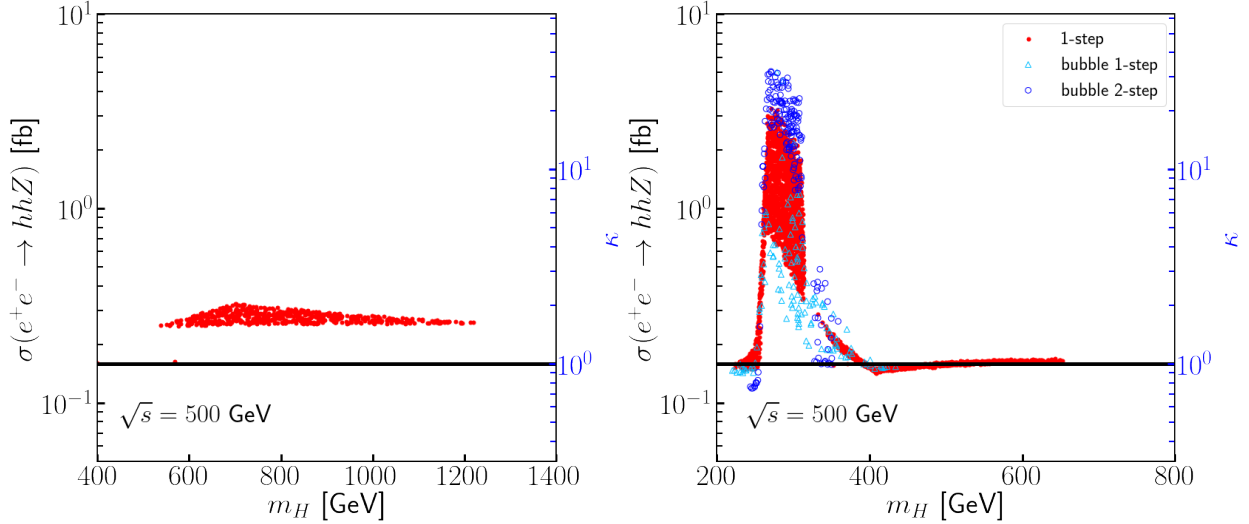
FIG. 15. The hhZ production at lepton collider in GM model.

FIG. 16. The unpolarized cross section of $e^+e^- \rightarrow hhZ$ at $\sqrt{s} = 500$ GeV for $H5$ -plane (left) and low mass benchmark (right) with one-step (red points) and two-step (blue points) EWPT. The horizontal line indicates the SM value. The secondary y-axis in the right-hand side of each plot indicates $\kappa \equiv \frac{\sigma^{GM}}{\sigma_{SM}}$. The blue points are further separated into two categories: “bubble one-step” (light blue triangle) and “bubble two-step” (dark blue circle).

There are also proposals focusing on the electron colliders aiming at the Higgs properties measurements. These lepton colliders also provide another opportunity to search the Higgs pair production [62]. Hence, we also investigate the sensitivity of the Higgs pair production at the lepton collider associated with Z -boson for $H5$ -plane and low mass benchmark. The corresponding processes are shown in Fig. 15. The cross sections are calculated using `MadGraph` and the same model files as mentioned above. The SM cross section of such process peaks around $\sqrt{s} = 500$ GeV. To maximize the possible sensitivity, we thus focus on the 500 GeV scenario of the lepton collider.

The unpolarized total cross sections are shown in Fig. 16 for $H5$ -plane (left panel) and low mass benchmark (right panel). The enhancement factor $\kappa = \frac{\sigma^{GM}}{\sigma_{SM}}$ is also indicated in the secondary y-axis in the right-hand side of each plot. We find that in $H5$ -plane, the cross section has a moderate enhancement with $\kappa \sim 2$ for the entire viable points. However, in low mass benchmark, κ spans

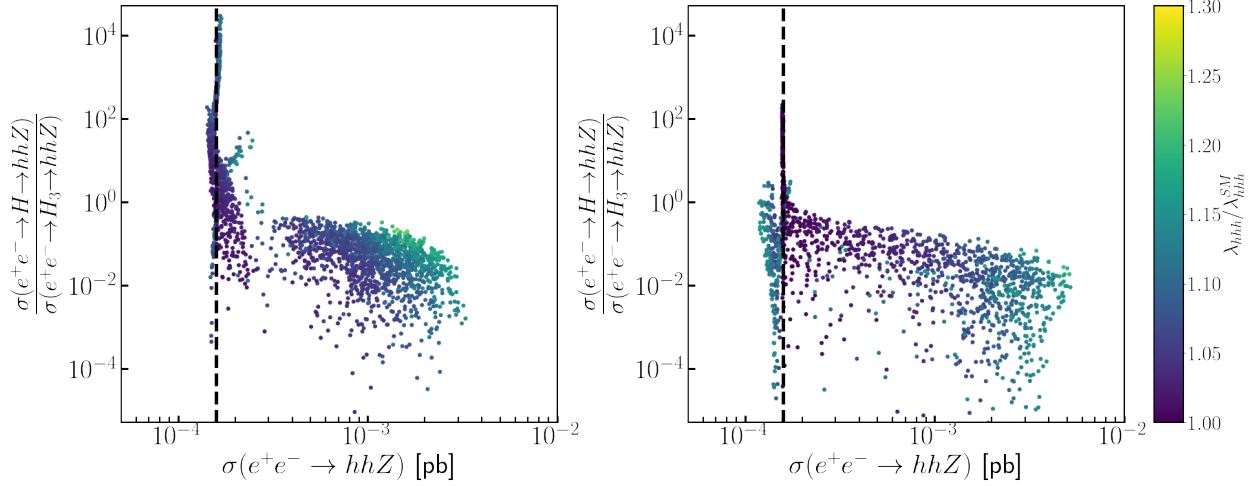


FIG. 17. The ratio between H and H_3 induced the cross section with respect to the total cross section in *low mass benchmark* for one-step (left) and two-step (right) SFOEWPT.

a large range, and can even reach about 30 for mass around 300 GeV. For *H5plane*, the moderate enhancement mainly comes from the large λ_{hhh} , as the collision energy is not enough for the resonance production through either H or H_3 . While, in the low mass benchmark, these masses are within the reach of the collision energy, the resonance production of H and/or H_3 induce the huge enhancement.

Fig. 17 shows the ratio between H and H_3 induced the cross section with respect to the total cross section in *low mass benchmark* for both one-step (left) and two-step (right) cases. It is clear that the enhancement in the total cross section mainly comes from H_3 resonance in *low mass benchmark*. When the collision energy raise to even higher value, it is also possible, in *H5plane*, to enhance the Higgs pair production through H_3 and/or H resonance. With the high precision that we can achieve for the cross section measurement at the ILC/CEPC, these machines will have sensitivity for these SFOEWPT viable points.

To give a more concrete sensitive study of such channel, the polarized cross sections are also calculated for $P(e^-, e^+) = (-80\%, 30\%)$ and $P(e^-, e^+) = (80\%, -30\%)$. We combine the sensitivities from $bbbb$ and $bbWW$ channels of this process from [63, 64] to obtain the constraints in the σ_{RL} - σ_{LR} plane which is shown in Fig. 18. From this plot, we find that the almost all the SFOEWPT viable points in *H5plane* can be excluded by this measurement. In the low mass benchmark, most points can also be excluded. However, we still have both one-step and two-step SFOEWPT viable points that are beyond the sensitivity in *low mass benchmark*.

Some other channels are also possible as a complimentary to the GW signal, especially for lower mass region. In [31], authors studied the sensitivities from the loop-induced channel $W\gamma$ from fermiophobic scalar which is specific for *low mass benchmark*. On the other hand, the diphoton searches [65, 66] are also promising. However, after re-interpret the bounds from [31] in our case, we found that they are not yet sensitive to reach the SFOEWPT viable points. Further improvement and detailed studies are needed for these searches.

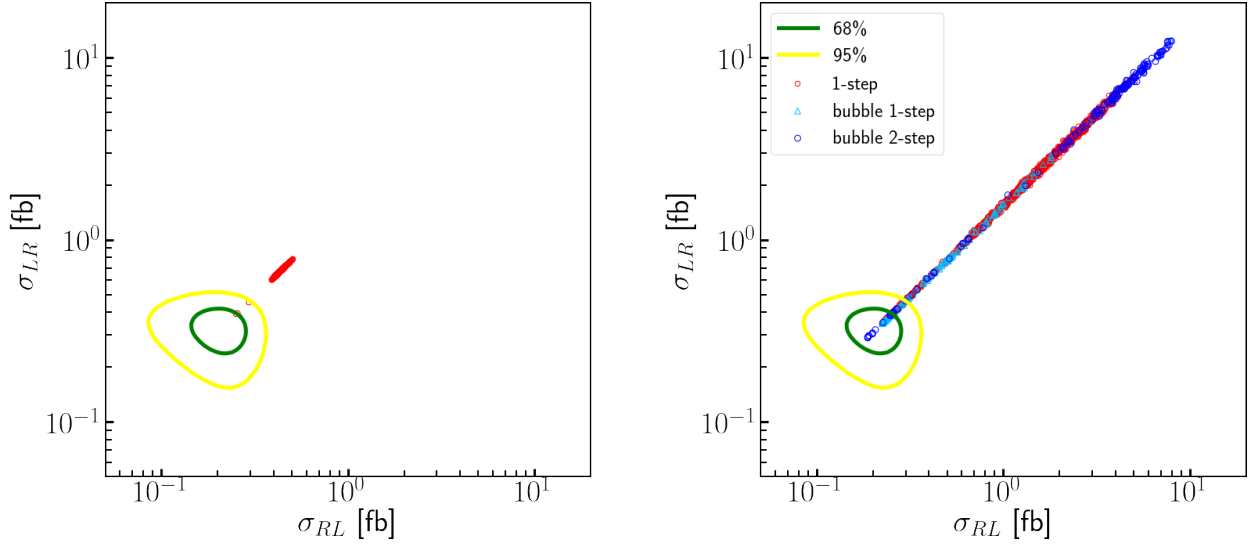


FIG. 18. The constraints of the polarized hhZ production cross section measurement in the σ_{RL} - σ_{LR} plane for H5-plane (left) and low mass benchmark (right). The red and blue points are the one-step and two-step viable points in the GM parameter space respectively. The green and yellow lines are the 68% and 95% C.L. contour respectively. The blue points are further separated into two categories: “bubble one-step” (light blue triangle) and “bubble two-step” (dark blue circle).

In xSM, the high mass region of the extra Higgs is not going to be covered by Higgs pair production searches at the future HL-LHC, and a lot parameter spaces there are not going to be probed by the diboson searches due to the small mixing angle of the SM Higgs and the heavy extra Higgs suppress effect. These regions can be complementary searched by the gravitational wave space-based detectors [29]. At the ILC, the Higgs pair search results are shown in Fig. 19, where the cross sections are obtained using the same method as in GM model. We find that in xSM model, the cross sections (unpolarized or polarized) has moderate enhancement. From the prospects of the future cross section measurement, we could exclude most one-step as well as two-step points in xSM.

In Fig. 20, we show the future hadron and lepton colliders sensitivity to the parameter spaces of one-step and two-step SFOEWPT for *H5plane* and *low mass benchmark* from the Higgs signal strength measurement, the conventions are the same as those in Fig. 8. Here, all the curves are obtained by fitting the SM-like Higgs signal strength measurement from each experiments prospects (LHC [67–74], CEPC [75], ILC [76] and FCC-ee [77, 78]). From Fig. 20, we find that, most one-step points in both *H5plane* and *low mass benchmark* can be excluded by the Higgs signal strength measurements. While we still have a bunch of points for the two-step case locating around the alignment limit and escaping the signal strength measurements. The stochastic GWs can be detected by finding the cross correlation of two independent interferometers (SNR) [50], we calculate the quantity for LISA and the $SNR > 10$ points mostly concentrate in the region of a large v_ξ of the *low mass benchmark*.

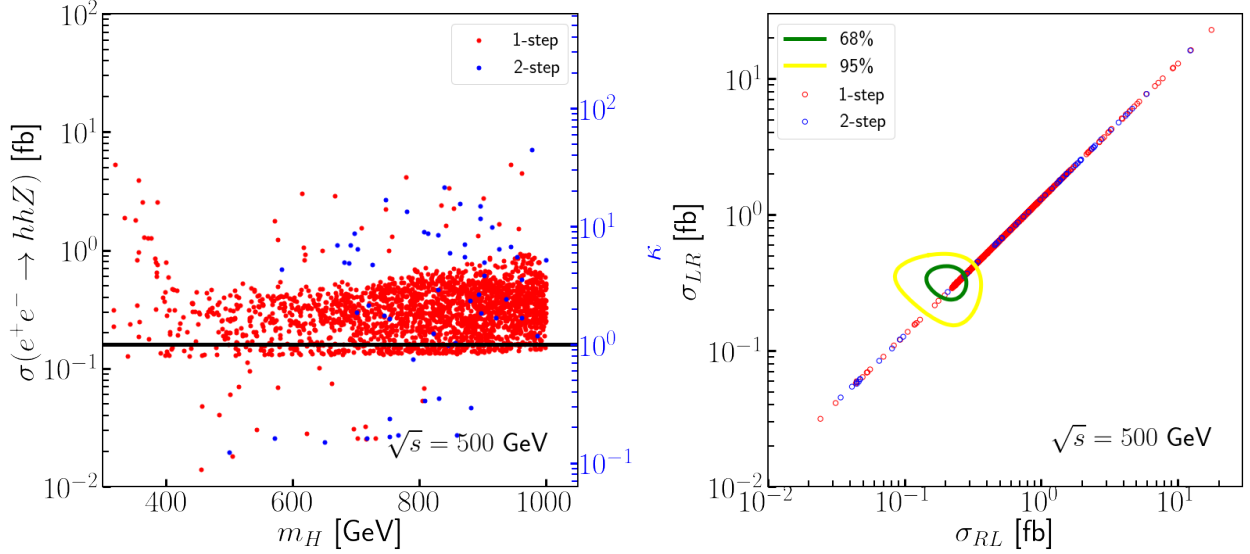


FIG. 19. The unpolarized cross section of $e^+e^- \rightarrow hhZ$ at $\sqrt{s} = 500$ GeV (left) and the constraints of the polarized hhZ production cross section measurement in the σ_{RL} - σ_{LR} plane (right) for xSM.

We finally present the future colliders sensitivities in the SFOEWPT parameter spaces, with an conservative consideration where only the deviation of the SM couplings are included. We first show in Fig. 21 the measurements of the two couplings (λ_{hhh} and λ_{hhhh}) at future e^+e^- colliders and the HL-LHC. Ref. [79] provides the 68%CL and 95%CL results (the inner and outer horizontal bar regions) of the future e^+e^- colliders and HL-LHC measurements, though which only include the cubic coupling in their analysis based on effective field theory approach. Another future ILC measurements precision (brown and blue lines) are adopted from Ref. [52], where the analysis are also based on effective field theory approach, and therefore we expect the UV model search would provide much better prediction. For the situation with additional EWSB contributions, i.e., the GM model, we expect the future lepton hadron collider be more powerful, since the phase transition possibility would be highly restricted by collider searches, especially the diboson search.

VI. CONCLUSIONS

Utilizing the Georgi-Machacek (GM) model, we simultaneously study Higgs phenomenology and the Electroweak phase transition for the scenario with the eEWSB contribution. The eEWSB is found to be helpful to realize different vacuum structure from the SM as the Universe cools down, and therefore leads to different strongly first order Electroweak phase transition patterns. We explore two benchmarks of the Georgi-Machacek (GM) to demonstrate the point. For both the one-step and the two-step SFOEWPT, we performed the study of the gravitational wave searches and the Higgs pair searches of the cubic Higgs couplings at hadronic and leptonic colliders. For comparison, we present the xSM model to show the situation without eEWSB. We found that: 1) most of the SFOEWPT parameter spaces is able to be covered by the future lepton colliders; 2)

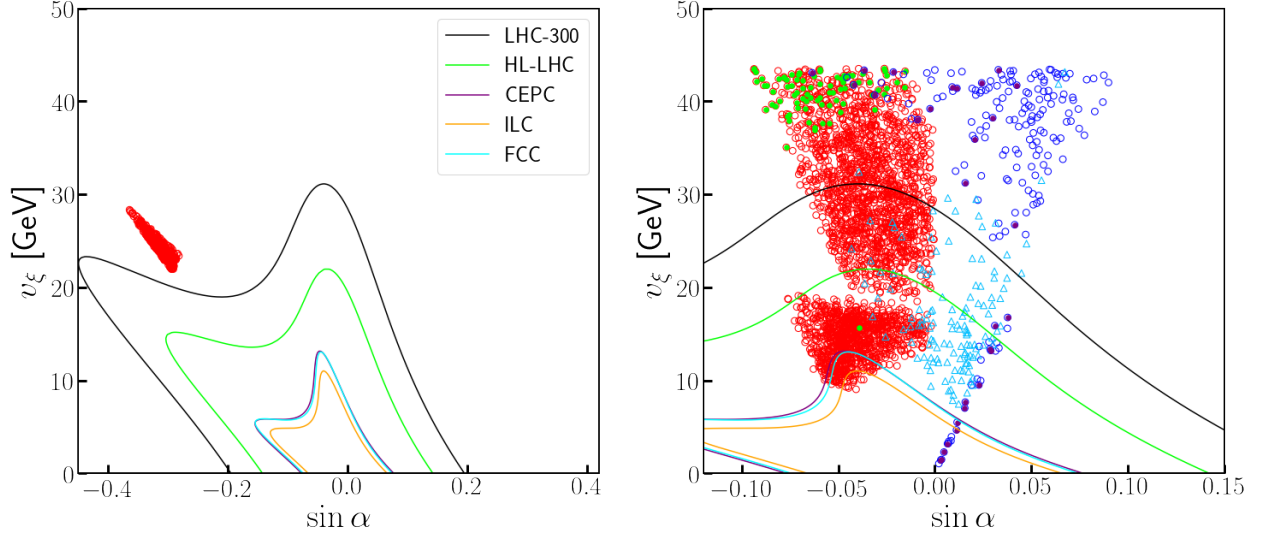


FIG. 20. The SFOEWPT viable points (bubble nucleation can occur and $v_n/T_n > 1$) in the $\sin\alpha$ - v_ξ plane for one-step (red) and two-step (blue) phase transition for *H5plane* (left panel) and *low mass benchmark* (right panel) scenario. The contours with different colors represent the constraints from the Higgs precision measurement from different experiments as indicated in the legend. In *low mass benchmark*, we also indicate the points having $SNR > 10$ with solid markers for one-step (green) and two-step (purple) cases.

the GWs mostly come from the second-step SFOEWPT in the GM model. 3) in comparison with the xSM model, the GW signals (to be probed by LISA) from the SFOEWPT of the GM model requires much higher precision of the colliders.

ACKNOWLEDGMENT

We thank Yi Liao, Zhi-Long Han and Bin Li for helpful discussions. The work of LGB is Supported by the National Natural Science Foundation of China (under grant No.11605016 and No.11647307), Basic Science Research Program through the National Research Foundation of Korea (NRF) funded by the Ministry of Education, Science and Technology (NRF-2016R1A2B4008759), and Korea Research Fellowship Program through the National Research Foundation of Korea (NRF) funded by the Ministry of Science and ICT (2017H1D3A1A01014046). The work of Y.C.W. is partially supported by the Natural Sciences and Engineering Research Council of Canada. H.G. is supported in part by the U.S. Department of Energy grant ds-sc0009956.

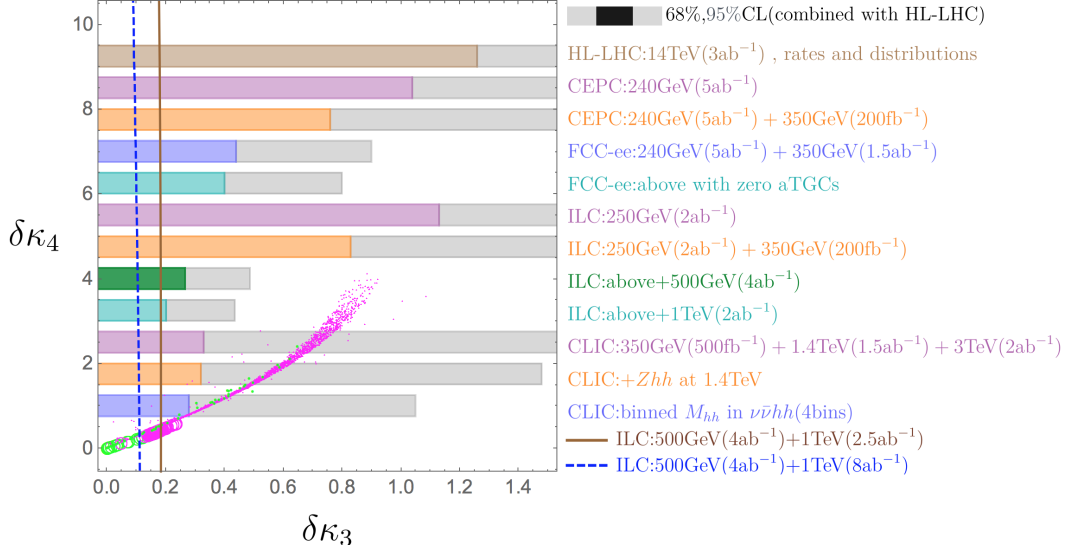


FIG. 21. Collider sensitivities of the triple Higgs coupling and quartic higgs coupling with the $SNR > 10$ points. The green and magenta represent the two-step and one-step SFOEWPT points. The circle points and the dotted points represent the GM and xSM model scenarios. The bars and contours are the sensitivities taken from Ref. [52, 79].

Appendix A: The GM model

In the Georgi-Machacek model, there are one isospin doublet scalar field $\phi = (\phi^+, \phi^0)^T$ with hypercharge $Y = \frac{1}{2}$, one complex isospin triplet scalar field $\chi = (\chi^{++}, \chi^+, \chi^0)^T$ with hypercharge $Y = 1$, and one real triplet $\xi = (\xi^+, \xi^0, -\xi^{+*})^T$ with hypercharge $Y = 0$. The custodial symmetry is introduced at tree level by imposing a global $SU(2)_L \times SU(2)_R$ symmetry upon the scalar potential. The neutral components of each fields can be parameterized into real and imaginary parts according to

$$\phi^0 = \frac{v_\phi + h_\phi + ia_\phi}{\sqrt{2}}, \quad \chi^0 = \frac{v_\chi + h_\chi + ia_\chi}{\sqrt{2}}, \quad \xi^0 = v_\xi + h_\xi, \quad (A1)$$

where v_ϕ , v_χ and v_ξ are the VEVs of ϕ^0 , χ^0 and ξ^0 , respectively. With only neutral components of this model, the potential reads:

$$V_0 = \frac{1}{4}(4h_\phi^4\lambda_1 + 2(h_\xi^2 + h_\chi^2)(m_2^2 + 2\lambda_2(h_\xi^2 + h_\chi^2)) + 2\lambda_3(2h_\xi^4 + h_\chi^4) + h_\phi^2(2m_1^2 + 4\lambda_4h_\xi^2 + h_\xi(2\sqrt{2}\lambda_5h_\chi + \mu_1) + h_\chi(4\lambda_4h_\chi + \lambda_5h_\chi + \sqrt{2}\mu_1)) + 12\mu_2h_\xi h_\chi^2). \quad (A2)$$

We can derive the EWSB vacuum through the minimization conditions:

$$\frac{\partial V_0}{\partial h_\phi} = \frac{\partial V_0}{\partial h_\chi} = \frac{\partial V_0}{\partial h_\xi} = 0, \quad (A3)$$

where the fields other than ϕ^0 , χ^0 and ξ^0 take zero VEV's. In this paper, the solution satisfying the relation $v_\chi = \sqrt{2}v_\xi$ is selected, by which the EWSB vacuum maintains the diagonal $SU(2)_V$ symmetry. Thus the parameter $\rho = m_W^2/(m_Z^2 \cos \theta_w^2) = 1$ is established at the tree level. The W and Z boson masses from the EWSB give the constraint,

$$v_\phi^2 + 8v_\xi^2 \equiv v^2 = \frac{1}{\sqrt{2}G_F} \approx (246 \text{ GeV})^2. \quad (\text{A4})$$

When $v_\phi, v_\xi \neq 0$, with the help of Eq. (A3) (under the relation $v_\chi = \sqrt{2}v_\xi$), we could rewrite m_1^2, m_2^2 in terms of v_ϕ, v_ξ and other parameters in the Higgs potential as:

$$m_1^2 = -4\lambda_1 v_\phi^2 - 6\lambda_4 v_\xi^2 - 3\lambda_5 v_\xi^2 - \frac{3}{2}\mu_1 v_\xi, \quad (\text{A5})$$

$$m_2^2 = -12\lambda_2 v_\xi^2 - 4\lambda_3 v_\xi^2 - 2\lambda_4 v_\phi^2 - \lambda_5 v_\phi^2 - \mu_1 \frac{v_\phi^2}{4v_\xi} - 6\mu_2 v_\xi. \quad (\text{A6})$$

There are 13 scalar fields in this model. After diagonalizing the mass matrices, the fields can be rewritten as the physical scalars (quintuple, triplet and singlet respectively)

$$H_5^{++} = \chi^{++}, \quad H_5^+ = \frac{1}{\sqrt{2}}(\chi^+ - \xi^+), \quad H_5^0 = \sqrt{\frac{1}{3}}h_\chi - \sqrt{\frac{2}{3}}h_\xi, \quad (\text{A7})$$

$$H_3^+ = -\cos \theta_H \phi^+ + \sin \theta_H \frac{1}{\sqrt{2}}(\chi^+ + \xi^+), \quad H_3^0 = -\cos \theta_H a_\phi + \sin \theta_H a_\chi, \quad (\text{A8})$$

$$h = \cos \alpha h_\phi - \frac{\sin \alpha}{\sqrt{3}}(\sqrt{2}h_\chi + h_\xi), \quad H_1 = \sin \alpha h_\phi + \frac{\cos \alpha}{\sqrt{3}}(\sqrt{2}h_\chi + h_\xi), \quad (\text{A9})$$

and the goldstone bosons

$$G^+ = \sin \theta_H \phi^+ + \cos \theta_H \frac{1}{\sqrt{2}}(\chi^+ + \xi^+), \quad G^0 = \sin \theta_H a_\phi + \cos \theta_H a_\xi, \quad (\text{A10})$$

where $\sin \theta_H = \frac{2\sqrt{2}v_\xi}{v}$ and $\cos \theta_H = \frac{v_\phi}{v}$, and α is the mixing angle between two singlets which is determined by the mass matrix of these scalars as will be shown below.

The 3 goldstone bosons eventually become the longitudinal components of the W and Z bosons, while, the remaining 10 physical fields can be organized into a quintuple $H_5 = (H_5^{++}, H_5^+, H_5^0, H_5^-, H_5^{--})^T$, a triplet $H_3 = (H_3^+, H_3^0, H_3^-)^T$ and two singlets h and H_1 , where the former (h) is used to denote the SM-like Higgs boson. The triplet scalar is CP-odd, while others are CP-even. The masses of different multiplets can be written as

$$m_{H_5}^2 = m_{H_5^{\pm\pm}}^2 = m_{H_5^\pm}^2 = m_{H_5^0}^2 = (8\lambda_3 v_\xi^2 - \frac{3}{2}\lambda_5 v_\phi^2) - \frac{\mu_1 v_\phi^2}{4v_\xi} - 12\mu_2 v_\xi, \quad (\text{A11})$$

$$m_{H_3}^2 = m_{H_3^\pm}^2 = m_{H_3^0}^2 = -(\frac{\lambda_5}{2} + \frac{\mu_1}{4v_\xi})v^2. \quad (\text{A12})$$

The singlets masses of m_{h,H_1} are the eigenvalues of mass matrix written in terms of gauge eigenstates:

$$M^2 = \begin{pmatrix} M_{11}^2 & M_{12}^2 \\ M_{12}^2 & M_{22}^2 \end{pmatrix}, \quad (\text{A13})$$

with

$$M_{11}^2 = 8 \cos^2 \theta_H \lambda_1 v^2, \quad (\text{A14})$$

$$M_{22}^2 = \sin^2 \theta_H (3\lambda_2 + \lambda_3) v^2 + \cos^2 \theta_H M_1^2 - \frac{1}{2} M_2^2, \quad (\text{A15})$$

$$M_{12}^2 = \sqrt{\frac{3}{2}} \sin \theta_H \cos \theta_H [(2\lambda_4 + \lambda_5) v^2 - M_1^2], \quad (\text{A16})$$

where $M_1^2 = -\frac{v}{\sqrt{2} \sin \theta_H} \mu_1$ and $M_2^2 = -3\sqrt{2} \sin \theta_H v \mu_2$. The mixing angle α is determined by

$$\tan 2\alpha = \frac{2M_{12}^2}{M_{22}^2 - M_{11}^2}, \quad (\text{A17})$$

as a function of the θ_H .

Appendix B: EWPT in the SM + Real Singlet: xSM model

For the xSM model, the gauge invariant finite temperature effective potential is found to be [28, 29, 80]:

$$V(h, s, T) = -\frac{1}{2} [\mu^2 - \Pi_h(T)] h^2 - \frac{1}{2} [-b_2 - \Pi_s(T)] s^2 + \frac{1}{4} \lambda h^4 + \frac{1}{4} a_1 h^2 s + \frac{1}{4} a_2 h^2 s^2 + \frac{b_3}{3} s^3 + \frac{b_4}{4} s^4, \quad (\text{B1})$$

with the thermal masses given by

$$\begin{aligned} \Pi_h(T) &= \left(\frac{2m_W^2 + m_Z^2 + 2m_t^2}{4v^2} + \frac{\lambda}{2} + \frac{a_2}{24} \right) T^2, \\ \Pi_s(T) &= \left(\frac{a_2}{6} + \frac{b_4}{4} \right) T^2, \end{aligned} \quad (\text{B2})$$

Identifying the coefficient for terms with the same power of different fields, we could get the correspondence of the parameters in GM and xSM as listed in Tab. I.

Appendix C: The h^6 operator for GM and xSM models

The dimensional six operator h^6 can modify both cubic and quartic Higgs couplings, with the Higgs potential for the Higgs boson given by:

$$V_{SM+h^6}^h = -\frac{\mu_h^2}{2} h^2 + \frac{\lambda_h}{4} h^4 + \frac{1}{8\Lambda^2} h^6. \quad (\text{C1})$$

TABLE I. xSM convention vs GM convention

xSM	GM
$\frac{1}{24}T^2(a_2 + 3(3g^2 + g'^2 + 2Y_t^2 + 4\lambda)) - \mu^2$	$\frac{T^2}{8}(3g^2 + g'^2 + 16\lambda_1 + 12\lambda_4 + Y_t^2 \sec \theta_H) + m_1^2$
$b_2 + \frac{1}{12}(2a_2 + 3b_4)T^2$	$3m_2^2 + T^2(3g^2 + g'^2 + 11\lambda_2 + 7\lambda_3 + 2\lambda_4)$
λ	$4\lambda_1$
b_4	$12(3\lambda_2 + \lambda_3)$
a_2	$6(2\lambda_4 + \lambda_5)$
a_1	$3\mu_1$
b_3	$18\mu_2$

Here, the Λ indicates the scale where the heavy particles are integrated out. The minimization conditions lead to the following relations,

$$\mu_h^2 = \frac{m_h^2}{2} - \frac{3v^4}{4\Lambda^2}, \lambda = \frac{m_h^2}{2v^2} - \frac{3v^2}{2\Lambda^2}. \quad (\text{C2})$$

In this scenario, the requirement that the EW minimum being the global minimum leads to

$$\Lambda \geq v^2/m_h. \quad (\text{C3})$$

The cubic and quartic Higgs couplings are modified by the dimension-6 operator as

$$\lambda_{3h}^{h^6} = \frac{3m_h^2}{v} + \frac{6v^3}{\Lambda^2}, \lambda_{4h}^{h^6} = \frac{3m_h^2}{v^2} + \frac{36v^2}{\Lambda^2}. \quad (\text{C4})$$

The phase transition dynamics are estimated after taking into account the thermal correction of c_h , as in Ref. [33]. As studied in Ref. [32, 33], to obtain a SFOEWPT with the h^6 operators additional to the SM, the additional contribution to the quartic Higgs coupling λ should be compensate it's negative value and therefor to ensure the possibility of the SFOEWPT.

Suppose the extra Higgs is much heavy than the SM Higgs, the $(H^\dagger H)^3$ operator can be obtained after integrated out heavy Higgs in Fig. 22. For the GM model, the relevant interactions are given by,

$$\begin{aligned} \lambda_{2hH}^{GM} &= \frac{\sqrt{3}}{2} \cos \alpha (\mu_1 \cos \alpha^2 - 2 \sin \alpha^2 (\mu_1 - 4\mu_2)) \\ \lambda_{2h2H}^{GM} &= \cos 4\alpha (-3\lambda_1 - 3\lambda_2 - \lambda_3 + 3\lambda_4 + \frac{3\lambda_5}{2}) + 3\lambda_1 + 3\lambda_2 + \lambda_3 + \lambda_4 + \frac{\lambda_5}{2} \\ \lambda_{3H}^{GM} &= \frac{\sqrt{3}}{2} \cos \alpha (3\mu_1 \sin \alpha^2 + 8\mu_2 \cos \alpha^2). \end{aligned} \quad (\text{C5})$$

Using the equation of motion on Eq. (21), the coefficients of c_4, c_6, c_8 for the GM are obtained as follows,

$$\begin{aligned}
c_4^{GM} &= \lambda_1 \cos^4 \alpha + \sin^4 \alpha (\lambda_2 + \frac{\lambda_3}{3}) + \lambda_4 \sin^2 \alpha \cos^2 \alpha + \frac{1}{8} \lambda_5 \sin^2 2\alpha \\
&\quad - \frac{3 \cos^2 \alpha (\cos 2\alpha (8\mu_2 - 3\mu_1) + \mu_1 - 8\mu_2)^2}{128(m_1^2 \sin^2 \alpha + m_2^2 \cos^2 \alpha)} \\
c_6^{GM} &= \frac{1}{2048(m_1^2 \sin^2 \alpha + m_2^2 \cos^2 \alpha)^3} 3 \cos^2 \alpha (\cos 2\alpha (8\mu_2 - 3\mu_1) + \mu_1 - 8\mu_2)^2 \\
&\quad \times (4(m_1^2 \sin^2 \alpha + m_2^2 \cos^2 \alpha) (\cos 4\alpha (-6\lambda_1 - 6\lambda_2 - 2\lambda_3 + 6\lambda_4 + 3\lambda_5) \\
&\quad + 6\lambda_1 + 6\lambda_2 + 2\lambda_3 + 2\lambda_4 + \lambda_5) - \cos^2 \alpha (\cos 2\alpha (3\mu_1 - 8\mu_2) - \mu_1 + 8\mu_2) \\
&\quad \times (3\mu_1 \sin^2 \alpha + 8\mu_2 \cos^2 \alpha)) \\
c_8^{GM} &= \frac{1}{32768(m_1^2 \sin^2 \alpha + m_2^2 \cos^2 \alpha)^4} 3 \cos^4 \alpha (\cos 2\alpha (8\mu_2 - 3\mu_1) + \mu_1 - 8\mu_2)^4 \\
&\quad \times (3(8\lambda_1 \sin^4 \alpha + \sin^2 2\alpha (2\lambda_4 + \lambda_5)) + 8 \cos^4 \alpha (3\lambda_2 + \lambda_3)) .
\end{aligned} \tag{C6}$$

In the small mixing limit, above relations reduce to

$$\begin{aligned}
c_4^{GM} &= \lambda_1 - \frac{3\mu_1^2}{32m_2^2} + \frac{\alpha^2(3\mu_1^2 m_1^2 + 16m_2^4(-4\lambda_1 + 2\lambda_4 + \lambda_5) + 6\mu_1 m_2^2(3\mu_1 - 8\mu_2))}{32m_2^4} + O(\alpha^3) \\
c_6^{GM} &= \frac{3\mu_1^2(m_2^2(2\lambda_4 + \lambda_5) - \mu_1\mu_2)}{32m_2^6} + \frac{3\alpha^2\mu_1}{256m_2^8} (24\mu_1^2\mu_2 m_1^2 - \mu_1 m_2^2(3(\mu_1^2 - 24\mu_1\mu_2 + 64\mu_2^2) \\
&\quad + 16m_1^2(2\lambda_4 + \lambda_5)) + 8m_2^4(\mu_1(12\lambda_1 + 12\lambda_2 + 4\lambda_3 - 11(2\lambda_4 + \lambda_5)) + 16\mu_2(2\lambda_4 + \lambda_5))) \\
&\quad + O(\alpha^3) \\
c_8^{GM} &= \frac{3\mu_1^4(3\lambda_2 + \lambda_3)}{256m_2^8} + \frac{3\alpha^2\mu_1^3}{512m_2^{10}} (m_2^2(3\mu_1(-24\lambda_2 - 8\lambda_3 + 2\lambda_4 + \lambda_5) + 64\mu_2(3\lambda_2 + \lambda_3)) \\
&\quad - 8\mu_1 m_1^2(3\lambda_2 + \lambda_3)) + O(\alpha^3) .
\end{aligned} \tag{C7}$$

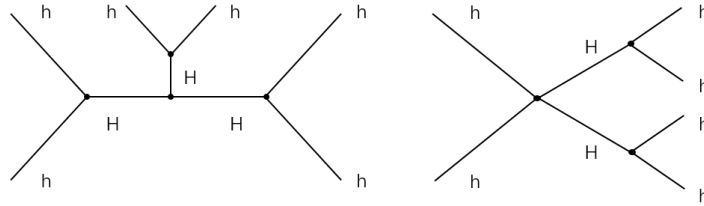


FIG. 22. The Feynman diagram for $(H^\dagger H)^3$ operator.

The cubic and quartic couplings relevant for the Fig. 22 in xSM are

$$\begin{aligned}\lambda_{2h2H}^{\text{xSM}} &= \frac{1}{4}(3(a_2 - b_4 - \lambda) \cos 4\alpha + a_2 + 3(b_4 + \lambda)) , \\ \lambda_{3H}^{\text{xSM}} &= \frac{3}{2}a_1 \sin \alpha^2 \cos \alpha + 2b_3 \cos \alpha^3 , \\ \lambda_{2hH}^{\text{xSM}} &= \frac{1}{2} \cos \alpha (a_1 \cos \alpha^2 - 2(a_1 - 2b_3) \sin \alpha^2) .\end{aligned}\quad (\text{C8})$$

As in the GM model, one can use the equation of motion upon Eq. (30) to obtain the coefficients of c_4, c_6, c_8 in xSM, as follows

$$\begin{aligned}c_4^{\text{xSM}} &= \frac{1}{4}(a_2 \sin^2 \alpha \cos^2 \alpha + b_4 \sin^4 \alpha + \lambda \cos^4 \alpha) - \frac{\cos^2 \alpha ((4b_3 - 3a_1) \cos 2\alpha + a_1 - 4b_3)^2}{128(b_2 \cos^2 \alpha - \mu^2 \sin^2 \alpha)} \\ c_6^{\text{xSM}} &= \frac{1}{1024(b_2 \cos^2 \alpha - \mu^2 \sin^2 \alpha)^3} \cos^2 \alpha ((4b_3 - 3a_1) \cos 2\alpha + a_1 - 4b_3)^2 \\ &\quad \times ((3 \cos 4\alpha (a_2 - b_4 - \lambda) + a_2 + 3(b_4 + \lambda))(b_2 \cos^2 \alpha - \mu^2 \sin^2 \alpha) \\ &\quad - \frac{1}{6} \cos \alpha ((3a_1 - 4b_3) \cos 2\alpha - a_1 + 4b_3)(3a_1 \sin^2 \alpha \cos \alpha + 4b_3 \cos^3 \alpha)) \\ c_8^{\text{xSM}} &= \frac{\cos^4 \alpha ((4b_3 - 3a_1) \cos 2\alpha + a_1 - 4b_3)^4 (a_2 \sin^2 \alpha \cos^2 \alpha + b_4 \cos^4 \alpha + \lambda \sin^4 \alpha)}{16384(b_2 \cos^2 \alpha - \mu^2 \sin^2 \alpha)^4} .\end{aligned}\quad (\text{C9})$$

In the small mixing limit, one has

$$\begin{aligned}c_4^{\text{xSM}} &= -\frac{a_1^2 - 8b_2\lambda}{32b_2} + \frac{\alpha^2(a_1^2(6b_2 - \mu^2) - 8a_1b_2b_3 + 8b_2^2(a_2 - 2\lambda))}{32b_2^2} + O(\alpha^3) \\ c_6^{\text{xSM}} &= -\frac{a_1^2(a_1b_3 - 3a_2b_2)}{192b_2^3} - \frac{\alpha^2a_1}{256b_2^4}(a_1^3b_2 + 4a_1^2b_3(\mu^2 - 3b_2) \\ &\quad + 4a_1b_2(a_2(11b_2 - 2\mu^2) - 6b_2(b_4 + \lambda) + 4b_3^2) - 32a_2b_2^2b_3) + O(\alpha^3) \\ c_8^{\text{xSM}} &= \frac{a_1^4b_4}{1024b_2^4} + \frac{a_1^3\alpha^2}{1024b_2^5}(a_1(a_2b_2 + 4b_4(\mu^2 - 3b_2)) + 16b_2b_3b_4) + O(\alpha^3)\end{aligned}\quad (\text{C10})$$

As studied in Ref. [81], the additional contribution to the h^4 can be reached, which captures the residual effects of the high dimension operators.

Up to now, we have calculated the high dimensional operators for the Higgs field by virtue of the method of CDE to match the UV models to the SMEFT [82]. These high dimensional operators, especially the $(H^\dagger H)^{3,4}$ are usually adopted to study phase transition in literatures. However, according to Fig. 23 which shows the distributions of m_1^2 and m_2^2 in both *H5plane* and *low mass benchmark*, the EFT approach does not apply for the GM model under study, especially the two-step case, as the basic assumption to integrate out the heavy degree of freedom is not fulfilled. The corresponding cases in xSM are also demonstrated in Fig. 24.

The light degree freedom fields are usually necessary for the multi-step phase transition, see Ref. [7, 10, 13–15, 17]. In this situation, one could not employ the the effective field theory (EFT) approach explored in literatures (e.g., [32, 33]) to study the phase transition. Even for the one-step phase transition, there are also some mismatch between the EFT approach and the UV complete

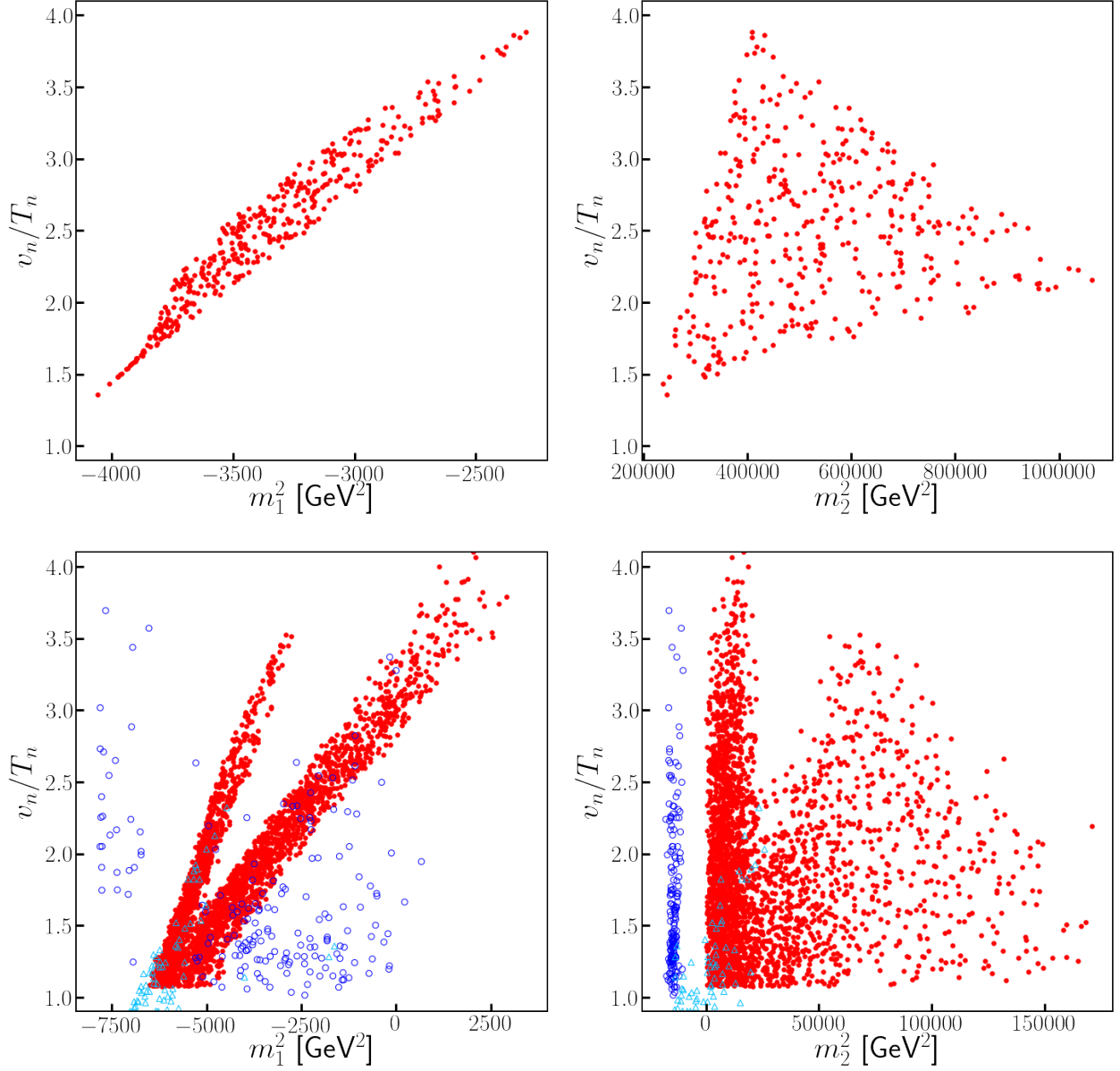


FIG. 23. The m_1^2 (left panels) and m_2^2 (right panels) distributions for *H5plane* (Top panels) and *low mass benchmark* (Bottom panels).

model studies, especially for the scenario where not so small mixing among the SM Higgs and extra Higgs are present, see the study of Ref. [83] for the “xSM” studies. We left the detailed survey on the match for the phase transition dynamics between UV complete models and EFT approach to further studies. Indeed, the EFT approach for integrated out heavy degree freedoms valid for negligible mixing situations.

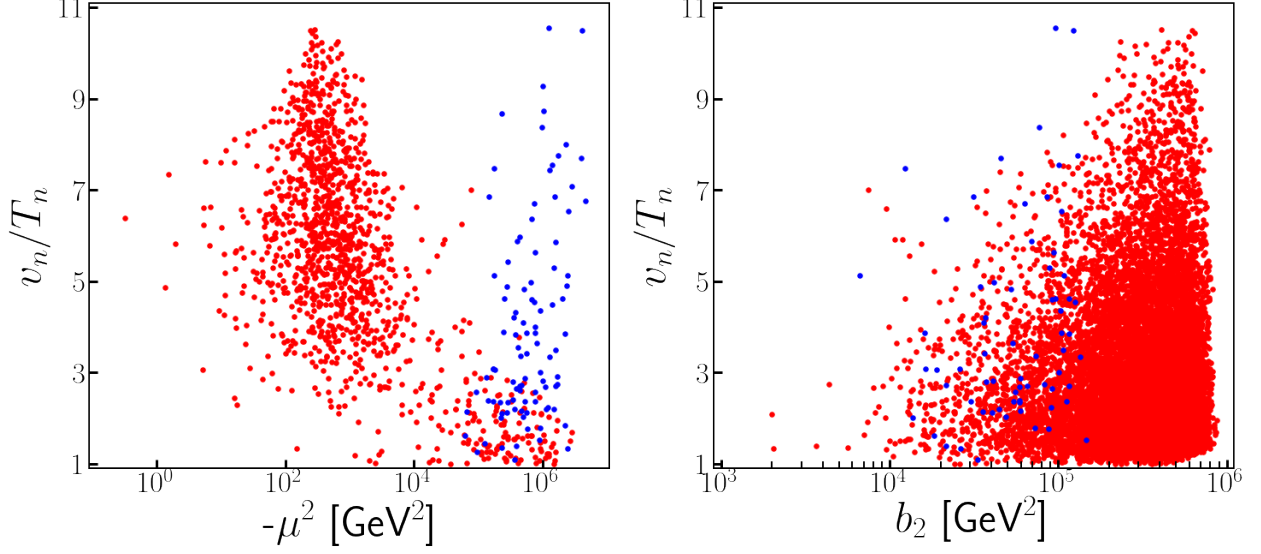


FIG. 24. The μ^2 and b_2 distributions of the one-step and two-step SFOEWPT valid points for xSM.

Appendix D: Some Couplings in GM model

$$g_{H_5^0 W^- W^+} = \frac{ie^2 v \sin(\theta_h) \bar{g}^{\rho\sigma}}{2\sqrt{3}s_W^2}, g_{H_5^0 ZZ} = -\frac{ie^2 v \sin(\theta_h) \bar{g}^{\rho\sigma}}{\sqrt{3}c_W^2 s_W^2}, \quad (D1)$$

$$g_{H_5^\mp W^\pm Z} = -\frac{ie^2 v \sin(\theta_h) \bar{g}^{\rho\sigma}}{2c_W s_W^2}, g_{H_5^{\mp\mp} W^\pm W^\pm} = \frac{ie^2 v \sin(\theta_h) \bar{g}^{\rho\sigma}}{\sqrt{2}s_W^2}, \quad (D2)$$

$$g_{HW^- W^+} = \frac{ie^2 v \sin(\alpha) \cos(\theta_h) \bar{g}^{\rho\sigma}}{2s_W^2} + \frac{i\sqrt{\frac{2}{3}}e^2 v \cos(\alpha) \sin(\theta_h) \bar{g}^{\rho\sigma}}{s_W^2}, \quad (D3)$$

$$g_{HZZ} = \frac{ie^2 v \sin(\alpha) \cos(\theta_h) \bar{g}^{\rho\sigma}}{2c_W^2 s_W^2} + \frac{i\sqrt{\frac{2}{3}}e^2 v \cos(\alpha) \sin(\theta_h) \bar{g}^{\rho\sigma}}{c_W^2 s_W^2}, \quad (D4)$$

$$g_{hW^- W^+} = \frac{ie^2 v \cos(\alpha) \cos(\theta_h) \bar{g}^{\rho\sigma}}{2s_W^2} - \frac{i\sqrt{\frac{2}{3}}e^2 v \sin(\alpha) \sin(\theta_h) \bar{g}^{\rho\sigma}}{s_W^2}, \quad (D5)$$

$$g_{hZZ} = \frac{ie^2 v \cos(\alpha) \cos(\theta_h) \bar{g}^{\rho\sigma}}{2c_W^2 s_W^2} - \frac{i\sqrt{\frac{2}{3}}e^2 v \sin(\alpha) \sin(\theta_h) \bar{g}^{\rho\sigma}}{c_W^2 s_W^2}, \quad (D6)$$

$$g_{H_3^0 h Z} = -\frac{\sqrt{\frac{2}{3}} e \sin(\alpha) \cos(\theta_h)}{c_W s_W} - \frac{e \cos(\alpha) \sin(\theta_h)}{2 c_W s_W}, \quad (\text{D7})$$

$$\begin{aligned} \lambda_{Hhh} = & -\frac{2i \sin(\alpha) \cos^2(\alpha) m_h^2 \sec(\theta_h)}{v} - \frac{2i \sqrt{\frac{2}{3}} \sin(\alpha) \sin(2\alpha) m_h^2 \csc(\theta_h)}{v} \\ & - \frac{i \sin(\alpha) \cos^2(\alpha) m_H^2 \sec(\theta_h)}{v} - \frac{i \sqrt{\frac{2}{3}} \sin(\alpha) \sin(2\alpha) m_H^2 \csc(\theta_h)}{v} \\ & - 2i\sqrt{2} \mu_1 \sin(\alpha) \cos^2(\alpha) \cot(\theta_h) + i\sqrt{2} \mu_1 \sin^3(\alpha) \cot(\theta_h) \\ & - i\sqrt{3} \mu_1 \sin(\alpha) \sin(2\alpha) \cot^2(\theta_h) + i\sqrt{3} \mu_2 \sin(\alpha) \sin(2\alpha), \end{aligned} \quad (\text{D8})$$

$$\begin{aligned} \lambda_{hhh} = & -\frac{3i \cos^3(\alpha) m_h^2 \sec(\theta_h)}{v} + \frac{2i \sqrt{6} \sin^3(\alpha) m_h^2 \csc(\theta_h)}{v} + 3i\sqrt{2} \mu_1 \sin^2(\alpha) \cos(\alpha) \cot(\theta_h) \\ & + 2i\sqrt{3} \mu_1 \sin^3(\alpha) \cot^2(\theta_h) - 2i\sqrt{3} \mu_2 \sin^3(\alpha). \end{aligned} \quad (\text{D9})$$

-
- [1] **ATLAS** Collaboration, G. Aad et al., *Observation of a new particle in the search for the Standard Model Higgs boson with the ATLAS detector at the LHC*, *Phys. Lett.* **B716** (2012) 1–29, [[arXiv:1207.7214](#)].
 - [2] **CMS** Collaboration, S. Chatrchyan et al., *Observation of a new boson at a mass of 125 GeV with the CMS experiment at the LHC*, *Phys. Lett.* **B716** (2012) 30–61, [[arXiv:1207.7235](#)].
 - [3] **LIGO Scientific, Virgo** Collaboration, B. P. Abbott et al., *Observation of Gravitational Waves from a Binary Black Hole Merger*, *Phys. Rev. Lett.* **116** (2016), no. 6 061102, [[arXiv:1602.03837](#)].
 - [4] **LIGO Scientific, Virgo** Collaboration, B. P. Abbott et al., *Upper Limits on the Stochastic Gravitational-Wave Background from Advanced LIGOs First Observing Run*, *Phys. Rev. Lett.* **118** (2017), no. 12 121101, [[arXiv:1612.02029](#)]. [Erratum: *Phys. Rev. Lett.* 119, no. 2, 029901 (2017)].
 - [5] A. D. Sakharov, *Violation of CP Invariance, C asymmetry, and baryon asymmetry of the universe*, *Pisma Zh. Eksp. Teor. Fiz.* **5** (1967) 32–35. [*Usp. Fiz. Nauk* 161, no. 5, 61 (1991)].
 - [6] D. E. Morrissey and M. J. Ramsey-Musolf, *Electroweak baryogenesis*, *New J. Phys.* **14** (2012) 125003, [[arXiv:1206.2942](#)].
 - [7] A. Alves, T. Ghosh, H.-K. Guo, and K. Sinha, *Resonant Di-Higgs Production at Gravitational Wave Benchmarks: A Collider Study using Machine Learning*, *JHEP* **12** (2018) 070, [[arXiv:1808.08974](#)].
 - [8] G. C. Dorsch, S. J. Huber, K. Mimasu, and J. M. No, *The Higgs Vacuum Uplifted: Revisiting the Electroweak Phase Transition with a Second Higgs Doublet*, *JHEP* **12** (2017) 086, [[arXiv:1705.09186](#)].
 - [9] C. P. D. Harman and S. J. Huber, *Does zero temperature decide on the nature of the electroweak phase transition?*, *JHEP* **06** (2016) 005, [[arXiv:1512.05611](#)].
 - [10] M. Jiang, L. Bian, W. Huang, and J. Shu, *Impact of a complex singlet: Electroweak baryogenesis and dark matter*, *Phys. Rev.* **D93** (2016), no. 6 065032, [[arXiv:1502.07574](#)].
 - [11] L. Bian, H.-K. Guo, and J. Shu, *Gravitational Waves, baryon asymmetry of the universe and electric dipole moment in the CP-violating NMSSM*, *Chin. Phys.* **C42** (2018), no. 9 093106, [[arXiv:1704.02488](#)].
 - [12] J. Bernon, L. Bian, and Y. Jiang, *A new insight into the phase transition in the early Universe with*

- two Higgs doublets, *JHEP* **05** (2018) 151, [[arXiv:1712.08430](#)].
- [13] W. Cheng and L. Bian, *Higgs inflation and cosmological electroweak phase transition with N scalars in the post-Higgs era*, *Phys. Rev.* **D99** (2019), no. 3 035038, [[arXiv:1805.00199](#)].
- [14] L. Bian and Y.-L. Tang, *Thermally modified sterile neutrino portal dark matter and gravitational waves from phase transition: The Freeze-in case*, *JHEP* **12** (2018) 006, [[arXiv:1810.03172](#)].
- [15] L. Bian and X. Liu, *Two-step strongly first-order electroweak phase transition modified FIMP dark matter, gravitational wave signals, and the neutrino mass*, *Phys. Rev.* **D99** (2019), no. 5 055003, [[arXiv:1811.03279](#)].
- [16] W. Chao, H.-K. Guo, and J. Shu, *Gravitational Wave Signals of Electroweak Phase Transition Triggered by Dark Matter*, *JCAP* **1709** (2017), no. 09 009, [[arXiv:1702.02698](#)].
- [17] W. Cheng and L. Bian, *From inflation to cosmological electroweak phase transition with a complex scalar singlet*, *Phys. Rev.* **D98** (2018), no. 2 023524, [[arXiv:1801.00662](#)].
- [18] R. Zhou, W. Cheng, X. Deng, L. Bian, and Y. Wu, *Electroweak phase transition and Higgs phenomenology in the Georgi-Machacek model*, *JHEP* **01** (2019) 216, [[arXiv:1812.06217](#)].
- [19] A. Klein et al., *Science with the space-based interferometer eLISA: Supermassive black hole binaries*, *Phys. Rev.* **D93** (2016), no. 2 024003, [[arXiv:1511.05581](#)].
- [20] H. Kudoh, A. Taruya, T. Hiramatsu, and Y. Himemoto, *Detecting a gravitational-wave background with next-generation space interferometers*, *Phys. Rev.* **D73** (2006) 064006, [[gr-qc/0511145](#)].
- [21] **TianQin** Collaboration, J. Luo et al., *TianQin: a space-borne gravitational wave detector*, *Class. Quant. Grav.* **33** (2016), no. 3 035010, [[arXiv:1512.02076](#)].
- [22] X. Gong et al., *Descope of the ALIA mission*, *J. Phys. Conf. Ser.* **610** (2015), no. 1 012011, [[arXiv:1410.7296](#)].
- [23] C.-W. Chiang and T. Yamada, *Electroweak phase transition in Georgi-Machacek model*, *Phys. Lett.* **B735** (2014) 295–300, [[arXiv:1404.5182](#)].
- [24] H. H. Patel and M. J. Ramsey-Musolf, *Baryon Washout, Electroweak Phase Transition, and Perturbation Theory*, *JHEP* **07** (2011) 029, [[arXiv:1101.4665](#)].
- [25] C. L. Wainwright, *CosmoTransitions: Computing Cosmological Phase Transition Temperatures and Bubble Profiles with Multiple Fields*, *Comput. Phys. Commun.* **183** (2012) 2006–2013, [[arXiv:1109.4189](#)].
- [26] K. Hartling, K. Kumar, and H. E. Logan, *The decoupling limit in the Georgi-Machacek model*, *Phys. Rev.* **D90** (2014), no. 1 015007, [[arXiv:1404.2640](#)].

- [27] **CMS Collaboration**, A. M. Sirunyan et al., *Observation of electroweak production of same-sign W boson pairs in the two jet and two same-sign lepton final state in proton-proton collisions at $\sqrt{s} = 13$ TeV*, *Phys. Rev. Lett.* **120** (2018), no. 8 081801, [[arXiv:1709.05822](#)].
- [28] S. Profumo, M. J. Ramsey-Musolf, C. L. Wainwright, and P. Winslow, *Singlet-catalyzed electroweak phase transitions and precision Higgs boson studies*, *Phys. Rev.* **D91** (2015), no. 3 035018, [[arXiv:1407.5342](#)].
- [29] A. Alves, T. Ghosh, H.-K. Guo, K. Sinha, and D. Vagie, *Collider and Gravitational Wave Complementarity in Exploring the Singlet Extension of the Standard Model*, *JHEP* **04** (2019) 052, [[arXiv:1812.09333](#)].
- [30] **LHC Higgs Cross Section Working Group Collaboration**, D. de Florian et al., *Handbook of LHC Higgs Cross Sections: 4. Deciphering the Nature of the Higgs Sector*, [arXiv:1610.07922](#).
- [31] H. E. Logan and Y. Wu, *Searching for the $W\gamma$ decay of a charged Higgs boson*, *JHEP* **11** (2018) 121, [[arXiv:1809.09127](#)].
- [32] C. Grojean, G. Servant, and J. D. Wells, *First-order electroweak phase transition in the standard model with a low cutoff*, *Phys. Rev.* **D71** (2005) 036001, [[hep-ph/0407019](#)].
- [33] P. Huang, A. Joglekar, B. Li, and C. E. M. Wagner, *Probing the Electroweak Phase Transition at the LHC*, *Phys. Rev.* **D93** (2016), no. 5 055049, [[arXiv:1512.00068](#)].
- [34] I. Affleck, *Quantum Statistical Metastability*, *Phys. Rev. Lett.* **46** (1981) 388.
- [35] A. D. Linde, *Decay of the False Vacuum at Finite Temperature*, *Nucl. Phys.* **B216** (1983) 421. [Erratum: *Nucl. Phys.* **B223**, 544 (1983)].
- [36] A. D. Linde, *Fate of the False Vacuum at Finite Temperature: Theory and Applications*, *Phys. Lett.* **100B** (1981) 37–40.
- [37] M. Hindmarsh, S. J. Huber, K. Rummukainen, and D. J. Weir, *Gravitational waves from the sound of a first order phase transition*, *Phys. Rev. Lett.* **112** (2014) 041301, [[arXiv:1304.2433](#)].
- [38] M. Hindmarsh, S. J. Huber, K. Rummukainen, and D. J. Weir, *Numerical simulations of acoustically generated gravitational waves at a first order phase transition*, *Phys. Rev.* **D92** (2015), no. 12 123009, [[arXiv:1504.03291](#)].
- [39] A. Kosowsky, M. S. Turner, and R. Watkins, *Gravitational radiation from colliding vacuum bubbles*, *Phys. Rev.* **D45** (1992) 4514–4535.
- [40] A. Kosowsky, M. S. Turner, and R. Watkins, *Gravitational waves from first order cosmological phase transitions*, *Phys. Rev. Lett.* **69** (1992) 2026–2029.

- [41] A. Kosowsky and M. S. Turner, *Gravitational radiation from colliding vacuum bubbles: envelope approximation to many bubble collisions*, *Phys. Rev.* **D47** (1993) 4372–4391, [[astro-ph/9211004](#)].
- [42] S. J. Huber and T. Konstandin, *Gravitational Wave Production by Collisions: More Bubbles*, *JCAP* **0809** (2008) 022, [[arXiv:0806.1828](#)].
- [43] R. Jinno and M. Takimoto, *Gravitational waves from bubble collisions: An analytic derivation*, *Phys. Rev.* **D95** (2017), no. 2 024009, [[arXiv:1605.01403](#)].
- [44] R. Jinno and M. Takimoto, *Gravitational waves from bubble dynamics: Beyond the Envelope*, *JCAP* **1901** (2019) 060, [[arXiv:1707.03111](#)].
- [45] D. Bodeker and G. D. Moore, *Can electroweak bubble walls run away?*, *JCAP* **0905** (2009) 009, [[arXiv:0903.4099](#)].
- [46] J. M. No, *Large Gravitational Wave Background Signals in Electroweak Baryogenesis Scenarios*, *Phys. Rev.* **D84** (2011) 124025, [[arXiv:1103.2159](#)].
- [47] J. R. Espinosa, T. Konstandin, J. M. No, and G. Servant, *Energy Budget of Cosmological First-order Phase Transitions*, *JCAP* **1006** (2010) 028, [[arXiv:1004.4187](#)].
- [48] C. Caprini, R. Durrer, and G. Servant, *The stochastic gravitational wave background from turbulence and magnetic fields generated by a first-order phase transition*, *JCAP* **0912** (2009) 024, [[arXiv:0909.0622](#)].
- [49] P. Binetruy, A. Bohe, C. Caprini, and J.-F. Dufaux, *Cosmological Backgrounds of Gravitational Waves and eLISA/NGO: Phase Transitions, Cosmic Strings and Other Sources*, *JCAP* **1206** (2012) 027, [[arXiv:1201.0983](#)].
- [50] C. Caprini et al., *Science with the space-based interferometer eLISA. II: Gravitational waves from cosmological phase transitions*, *JCAP* **1604** (2016), no. 04 001, [[arXiv:1512.06239](#)].
- [51] W. BizoA, U. Haisch, and L. Rottoli, *Constraints on the quartic Higgs self-coupling from double-Higgs production at future hadron colliders*, [arXiv:1810.04665](#).
- [52] T. Liu, K.-F. Lyu, J. Ren, and H. X. Zhu, *Probing the quartic Higgs boson self-interaction*, *Phys. Rev.* **D98** (2018), no. 9 093004, [[arXiv:1803.04359](#)].
- [53] O. J. P. Eboli, G. C. Marques, S. F. Novaes, and A. A. Natale, *TWIN HIGGS BOSON PRODUCTION*, *Phys. Lett.* **B197** (1987) 269–272.
- [54] T. Plehn, M. Spira, and P. M. Zerwas, *Pair production of neutral Higgs particles in gluon-gluon collisions*, *Nucl. Phys.* **B479** (1996) 46–64, [[hep-ph/9603205](#)]. [Erratum:

- Nucl.Phys.B531,655(1998)].
- [55] B. Hespel and E. Vryonidou, “<https://cp3.irmp.ucl.ac.be/projects/madgraph/wiki/HiggsPairProduction>.”
 - [56] A. Peterson, H. E. Logan, K. Hartling, K. Kumar, and Y. Wu, “<http://feynrules.irmp.ucl.ac.be/wiki/GeorgiMachacekModel>.”
 - [57] C. Degrande, *Automatic evaluation of UV and R2 terms for beyond the Standard Model Lagrangians: a proof-of-principle*, *Comput. Phys. Commun.* **197** (2015) 239–262, [[arXiv:1406.3030](https://arxiv.org/abs/1406.3030)].
 - [58] A. Alloul, N. D. Christensen, C. Degrande, C. Duhr, and B. Fuks, *FeynRules 2.0 - A complete toolbox for tree-level phenomenology*, *Comput. Phys. Commun.* **185** (2014) 2250–2300, [[arXiv:1310.1921](https://arxiv.org/abs/1310.1921)].
 - [59] J. Alwall, R. Frederix, S. Frixione, V. Hirschi, F. Maltoni, O. Mattelaer, H. S. Shao, T. Stelzer, P. Torrielli, and M. Zaro, *The automated computation of tree-level and next-to-leading order differential cross sections, and their matching to parton shower simulations*, *JHEP* **07** (2014) 079, [[arXiv:1405.0301](https://arxiv.org/abs/1405.0301)].
 - [60] K. Hartling, K. Kumar, and H. E. Logan, *GMCALC: a calculator for the Georgi-Machacek model*, [arXiv:1412.7387](https://arxiv.org/abs/1412.7387).
 - [61] J. Chang, C.-R. Chen, and C.-W. Chiang, *Higgs boson pair productions in the Georgi-Machacek model at the LHC*, *JHEP* **03** (2017) 137, [[arXiv:1701.06291](https://arxiv.org/abs/1701.06291)].
 - [62] B. Li, Z.-L. Han, and Y. Liao, *Higgs production at future e^+e^- colliders in the Georgi-Machacek model*, *JHEP* **02** (2018) 007, [[arXiv:1710.00184](https://arxiv.org/abs/1710.00184)].
 - [63] C. F. Durig, *Measuring the Higgs Self-coupling at the International Linear Collider*. PhD thesis, Hamburg U., Hamburg, 2016.
 - [64] M. Kurata and T. Tanabe, *The Higgs Self Coupling Analysis Using the Events Containing $H \rightarrow WW^*$ Decay*, Tech. Rep. LC-REP-2013-025, 2013.
 - [65] ATLAS Collaboration, G. Aad et al., *Search for Scalar Diphoton Resonances in the Mass Range 65 – 600 GeV with the ATLAS Detector in pp Collision Data at $\sqrt{s} = 8$ TeV*, *Phys. Rev. Lett.* **113** (2014), no. 17 171801, [[arXiv:1407.6583](https://arxiv.org/abs/1407.6583)].
 - [66] ATLAS Collaboration, M. Aaboud et al., *Search for new phenomena in high-mass diphoton final states using 37 fb⁻¹ of proton–proton collisions collected at $\sqrt{s} = 13$ TeV with the ATLAS detector*, *Phys. Lett.* **B775** (2017) 105–125, [[arXiv:1707.04147](https://arxiv.org/abs/1707.04147)].
 - [67] *Projections for measurements of Higgs boson signal strengths and coupling parameters with the*

- ATLAS detector at a HL-LHC*, Tech. Rep. ATL-PHYS-PUB-2014-016, CERN, Geneva, Oct, 2014.
- [68] *Projections for measurements of Higgs boson cross sections, branching ratios and coupling parameters with the ATLAS detector at a HL-LHC*, Tech. Rep. ATL-PHYS-PUB-2013-014, CERN, Geneva, Oct, 2013.
- [69] *HL-LHC projections for signal and background yield measurements of the $H \rightarrow \gamma\gamma$ when the Higgs boson is produced in association with t quarks, W or Z bosons*, Tech. Rep. ATL-PHYS-PUB-2014-012, CERN, Geneva, Jul, 2014.
- [70] *Update of the prospects for the $H \rightarrow Z\gamma$ search at the High-Luminosity LHC*, Tech. Rep. ATL-PHYS-PUB-2014-006, CERN, Geneva, May, 2014.
- [71] *Prospects for the study of the Higgs boson in the $VH(bb)$ channel at HL-LHC*, Tech. Rep. ATL-PHYS-PUB-2014-011, CERN, Geneva, Jul, 2014.
- [72] *Studies of the VBF $H \rightarrow \tau_l \tau_{had}$ analysis at High Luminosity LHC conditions*, Tech. Rep. ATL-PHYS-PUB-2014-018, CERN, Geneva, Oct, 2014.
- [73] C. Hartmann and M. Trott, *Higgs Decay to Two Photons at One Loop in the Standard Model Effective Field Theory*, *Phys. Rev. Lett.* **115** (2015), no. 19 191801, [[arXiv:1507.03568](#)].
- [74] T. ATLAS-collaboration, *Physics at a High-Luminosity LHC with ATLAS (Update)*, Tech. Rep. ATL-PHYS-PUB-2012-004, CERN, Geneva, Oct, 2012.
- [75] **CEPC Study Group** Collaboration, M. Dong et al., *CEPC Conceptual Design Report: Volume 2 - Physics & Detector*, [arXiv:1811.10545](#).
- [76] P. Bambade et al., *The International Linear Collider: A Global Project*, [arXiv:1903.01629](#).
- [77] **FCC** Collaboration, A. Abada et al., *Future Circular Collider*, .
- [78] **FCC** Collaboration, A. Abada et al., *Future Circular Collider*, .
- [79] S. Di Vita, G. Durieux, C. Grojean, J. Gu, Z. Liu, G. Panico, M. Riembau, and T. Vantalon, *A global view on the Higgs self-coupling at lepton colliders*, *JHEP* **02** (2018) 178, [[arXiv:1711.03978](#)].
- [80] J. Kozaczuk, *Bubble Expansion and the Viability of Singlet-Driven Electroweak Baryogenesis*, *JHEP* **10** (2015) 135, [[arXiv:1506.04741](#)].
- [81] M. Jiang, N. Craig, Y.-Y. Li, and D. Sutherland, *Complete One-Loop Matching for a Singlet Scalar in the Standard Model EFT*, *JHEP* **02** (2019) 031, [[arXiv:1811.08878](#)].
- [82] B. Henning, X. Lu, and H. Murayama, *How to use the Standard Model effective field theory*, *JHEP* **01** (2016) 023, [[arXiv:1412.1837](#)].
- [83] P. H. Damgaard, A. Haarr, D. O’Connell, and A. Tranberg, *Effective Field Theory and Electroweak*

Baryogenesis in the Singlet-Extended Standard Model, *JHEP* **02** (2016) 107,
[arXiv:1512.01963].